STUDY OF THZ SURFACE WAVES (TSW) ON

BARE AND COATED METAL SURFACE

By

GONG, MUFEI

Bachelor of Science in Optoelectronics
Tianjin University
Tianjin, China
1998

Master of Engineering
Nanyang Technological University
Singapore
2001

Submitted to the Faculty of the
Graduate College of the
Oklahoma State University
in partial fulfillment of
the requirements for
the Degree of
DOCTOR OF PHILOSOPHY
July, 2009

STUDY OF THZ SURFACE WAVES (TSW) ON

BARE AND COATED METAL SURFACE

Dissertation Approved:

Dr. Daniel Grischkowsky

Dissertation Adviser

Dr. R. Alan Cheville

Dr. Weili Zhang

Dr. Albert T. Rosenberger

Dr. A. Gordon Emslie

Dean of the Graduate College

ACKNOWLEDGMENTS

First of all, I want to express my appreciation to Dr. Daniel R. Grischkowsky, my major advisor, for giving me the chance to do my Ph. D. in one of the best THz group in the world and always guiding me with his scientific excellence and extremely high standard throughout my Ph. D. study. I am proud of the quality of the work we did together. It has been an honor to be a student of his. I am sure the training and scholarship I learned from Dr.G will keep benefiting me in my career.

I want to give my deep thanks to Dr. Weili Zhang, who is not only my committee member, but also the advisor of my undergraduate thesis in Tianjin University in China 11 years ago, for his continuous guidance, support and help to me all these years. I am grateful to all the trust, encouragement and friendship from Dr. Zhang.

I want to send my gratitude to my other current and former graduate committee members, Dr. Alan Cheville, Dr. Albert T. Rosenberger and Dr. Bret Flanders. All were very generous, with their time, patience and input. Special thanks to Dr. Cheville, who gave me a lot of important advices and offered me the facility to learn the new sample preparation technique.

I also want to thank Dr. Charles Bunting and Dr. James West, who have taught me and helped me to strengthen the electromagnetic part in my dissertation works.

Dr. Jianming Dai, Yuguang Zhao, Steve Coleman, Jiangquan Zhang, Matthew Reiten and Abul Azad, thank you for the training, advices and encouragement you gave to me when I first join the group.

During my hard time, I am so grateful that I have all of you: Adam Bingham, Norman Laman, Sree Harsha, Jiaguang Han, Xinchao Lu, Ranjan Singh, Suchira Ranmani, Yongyao Chen, Jianqiang Gu, Zhen Tian and Minh Dinh, all of you have been so supportive and willing to help. I will remember everyday I had with you and cherish our friendship.

To my parents, Chun’ai Guan and Chuan Gong, to all my family members and to my girlfriend, Yongfen Chen, words can never be enough to express my thankfulness to all the supports to me.

TABLE OF CONTENTS

Chapter Page

1. INTRODUCTION 1

1.1 Introduction of surface wave study.....1
1.2 Purpose of this study.....6
1.3 Scope of this report 7

2. EXPERIMENTAL SETUP.....10

3. EXPERIMENTAL RESULTS AND DISCUSSIONS 16

3.1 Individual signal.....16
3.1-1 Signal on bare metal surface.....17
3.1-2 Signal on dielectric coated surface 25
3.2 Signals taken above surface 28

4. THEORETICAL TREATMENT.....39

4.1 The surface wave field on bare metal surface.....39
4.2 The surface wave field on dielectric coated surface 41
4.2-1 The transverse field profile.....41
4.2-2 The dispersion.....46
4.2-3 The absorption coefficients 48
4.2-4 The coupling coefficients 53

5. CONCLUSIONS.....62

6. FUTURE WORK.....64

REFERENCES 65

APPENDICES 70
Appendix I 70
Appendix II 78

Appendix III.....80

LIST OF TABLES

Table Page

1-1 Evanescent Field Extent 4

LIST OF FIGURES

Figure Page

2-1 2D schematic of the system setup.....11

2-2 3D schematic of surface wave apparatus.....12

2-3 The optical part of the receiver.....13

3-1 Reference signal 16

3-2 Surface wave pulse on bare metal surface.....18

3-3 The diffraction pattern for 0.5 THz, λ = 600 µm.....20

3-4 Overlap integral at different distances.....22

3-5 Overlapping of the surface wave field pattern and the diffraction pattern.....23

3-6 THz surface wave pulse on dielectric coated surface with block.....26

3-7 TSW pulse on coated surface 27

3-8 THz surface wave pulses measured at the surface and at 0.6 mm above surface 29

3-9 Comparison of signals measured at the surface and above surface.....30

3-10 The time domain surface waveforms above dielectric-coated surface with block 31

3-11 Amplitude fall-off viewed in frequency domain 32

3-12 Unnormalized frequency dependent field fall-off curves.....33

3-13 Experimental surface wave fall-off 34

3-14 Theoretical fall-off on bare surface 36

3-15 Experimental and theoretical surface wave fall-off on coated surface.....37

3-16 Comparison of theoretical and experimental amplitude fall-off at selected frequencies 38

4-1 Theoretical model equivalence of slab waveguide structure.....42

4-2 left: E_y field TM_0 distribution at 0.5 THz of a plastic slab waveguide; right: field profile of coated surface (half of the field of the left).....43

4-3 Theoretical normalized surface wave fall-off curve 45
4-4 Exponential field fall-off constants calculated with and without perfect conductor assumption 45
4-5 Group velocity and phase velocity ratio to speed of light of the fundamental TM_0 mode of dielectric slab waveguide with a thickness of 25μm and an index of refraction of 1.5.....48
4-6 Fraction of power (η) at different frequencies in our surface structure.....49
4-7 Amplitude absorption due to the dielectric layer.....50
4-8 Amplitude absorption due to metal $\alpha_m/2$ using analytical method 52
4-9 Metal amplitude absorption calculated using approximation method.....53
4-10 Zoomed drawing of the PPWG-Surface wave junction 55
4-11 Electric field functions of the two coupling modes.....55
4-12 The calculated amplitude coupling coefficient of PPWG – SWG junction 56
4-13 Schematic of the wave propagation at the slit 57
4-14 Electric field function of the two coupling modes at the slit.....58
4-15 The calculated amplitude coupling coefficient of the slit.....59
4-16 The theoretical output spectrum and experimental output spectrum.....60
4-17 The comparison of the time domain curves between experiment and theory ..61

Chapter 1 Introduction

1.1 Introduction of surface wave study

Surface waves, which are also called surface plasma polaritons or surface plasmons, are the propagation modes of an electromagnetic wave which is bounded to the interface between two mediums. Different terms are used for emphasis on either the quantum or wave nature. In this study, because in the THz range the wave property is the main aspect of interest, surface waves will be the most appropriate terminology. The surface wave propagates along the interface while in the normal direction it has exponential decay on both sides of the interface (evanescent waves). To satisfy this condition, the dielectric constant of one of the mediums must be negative. Therefore, the surface wave is mostly studied on the surface of metal or doped semiconductors. As a solution of Maxwell's equations on the medium boundary, the form and the evanescent properties of the surface wave has a great dependency upon the surface morphology and the ambient dielectric distribution [2].

The earliest study of surface waves can be traced back to 100 years ago [3]. Since Sommerfeld and Zenneck [4] did the groundbreaking work on studying surface waves on a cylindrical surface and flat surface, theoretical models have been successfully built to

understand surface waves since the early 20th century. However, because of the limited availability of experimental techniques in the early days, the experimental study developed slowly. Especially the fundamental studies which mainly includes source, coupling configuration, propagation property, de-coupling configuration and detection are technically difficult in practice.

Technology advances in other fields promoted the research of the surface wave in some aspects. The surface wave was first studied in radio frequency range [5, 6]. In the 1960s, after the invention of laser, which provided a new type of light wave source, people started to study the surface plasmon in the optical range. The development of semiconductor devices provided sensors for the detection. The coupling, de-coupling and propagation of the surface wave were the first missions for surface wave researchers. To couple a freely propagating wave into the surface wave, aperture launching was used first [6]. In 1968, Otto proposed the prism coupling/decoupling method based on frustrated total internal reflection [7]. Raether discussed the feasibility of utilizing the surface roughness for the coupling and decoupling [8]. A lot of progress was made as technology further advanced. Especially in recent years, thanks to the major development in microchip fabrication and near-field techniques, researchers are able to study experimentally and to manipulate the propagation characteristics of surface waves. People have used bent, thin film coatings, periodic structures and corrugated surfaces to control the coupling, propagating and decoupling process of surface waves [9-11]. Numerous investigations have been carried out on the development of new optoelectronic devices, based on the evanescent property of surface waves. The potential applications

include bio-material analysis and spectroscopy, near-field microscopy, high density optical data storage and optical displays.

The propagation of surface waves was also extensively studied in theory; however, the experiments are difficult to realize because the direct measurement of the bounded (evanescent) field is difficult in practice. Surface waves have great dependency to the dielectric constants of the metal and the dielectric on the metal surface. From optical to the far infrared and THz range, the frequency dependent metal dielectric constant $\varepsilon_m = \varepsilon_m' + i\ \varepsilon_m''$ undergoes drastic change (see appendix II). The difference in metal conductivity and the consequent metal dielectric constant results in the significant changes of the surface waves in different frequency ranges.

In optical and near infrared range, according to Drude's theory, metal conductivity has small real part and big imaginary part which makes the metal a lossy medium. As a result, surface waves have small spatial evanescent extension in the air δ_{air} and in the metal δ_{metal} (the distance where the field drops to 1/e of the surface) and short propagation length L_i (the length at which the intensity drops to 1/e), relative to its wavelength as shown in comparison table below. Therefore, once an optical wave is coupled into the surface wave, the energy is confined to vicinity of the surface with a relatively short propagation length. The tightly bound surface wave field in the optical frequency range is difficult to detect directly. Therefore, the traditional way of studying surface wave in optical range is first to couple the wave into free space and detect from far field, and then to use theoretical method to retrieve or reconstruct the field on surface. For the direct

measurement of the field, the near-field scanning optical microscope could be a promising technique for the detection of surface fields [12].

On the other hand, in the microwave and THz range, the real part of metal conductivity is very high and is equal to its handbook dc value for aluminum, $\sigma_r = 4 \times 10^7$ S/m (the corresponding conductivity at optical frequencies at $\lambda = 800$ nm, $\sigma_r = 1.2 \times 10^5$ S/m). The real part of metal dielectric constant is a negative constant, while the much larger imaginary part is proportional to the wavelength.

Table 1-1. Evanescent Field Extent

	0.5 THz (λ=600)			1 THz (λ=300 μm)			375 THz (λ=800 nm)		
	δ_{air}	δ_{metal}	L_i	δ_{air}	δ_{metal}	L_i	δ_{air}	δ_{metal}	L_i
Al	160 mm	111 nm	137 m	56 mm	78 nm	34 m	1.27 μm	12.6 nm	235 μm
Ag	189 mm	87 nm	210 m	63 mm	59 nm	53 m	0.68 μm	23 nm	267 μm
Au	158 mm	107 nm	141 m	54 mm	74 nm	35 m	0.61 μm	25 nm	117 μm

The spatial extensions δ_{air} and δ_{metal} of the evanescent field and the propagation length L_i of the surface wave increase when the conductivity increases. Therefore in THz range, because metals have high conductivity and behave close to ideal lossless conductor, large spatial extension and propagation lengths are expected as shown in the table below. The

field extends into the air many hundreds of wavelengths. The low loss also enables the surface wave to propagate for tens of meters.

However, as the conductivity increases, the surface field extends so far into free space that the surface of the conductor has little confinement to the mode of surface wave. In fact, as it had been pointed out by many early researchers, in THz and the equivalent far infrared, the surface wave is difficult to build up on surface because it is so loosely bound to the surface, that coupling and decoupling occurs simultaneously along the long propagation length [13]. A solution to this problem is to cover the surface of the conductor with a thin layer of dielectric or to corrugate the surface such as using gratings. With the enhanced confinement introduced by these structures, the surface electromagnetic wave can be established. In 1950, Goubau [14] and Attwood [15] predicted the surface wave confinement in dielectric coated cylindrical wire and plane surface of perfect conductor, respectively. According to Attwood's analysis of the coated perfect conductor, the field has a trigonometric form inside the film and an exponential form outside in the vacuum. In 1953, Barlow and Cullen did an excellent overview of the surface wave studies in the early half of 20th century [5, 6]. In their works, surface waves at radio frequencies are discussed in detail.

The effect of coating dielectric films and gratings were further studied. In optical range, Schlesinger et al experimentally studied the far infrared surface plasmon propagation at 119 μm on germanium coated gold and lead surface [16]. In 1982, Stegeman analyzed Schlesinger's experiment in theory by assigning the substrate metal a finite value of

dielectric constant [17]. More detailed and generalized theoretical study of absorbing layers in microwave range have been carried out [18-22]. The grating and corrugation in microwave and infrared were also studied [23, 24].

THz surface wave (TSW) study was only started in recent years. Researchers applied techniques in both microwaves and optics to study surface waves. Both the THz Sommerfeld and Zenneck waves have been studied experimentally [25, 26]. THz surface propagation using lens coupling has been achieved [27]. Extraordinary THz transmission through subwavelength hole arrays has been observed and theoretically explained [28, 29]. The coupling and confinement of TSW using gratings and periodic surface structure have been extensively studied, exciting results were obtained [10, 30-33].

1.2 Purpose of this study

Success on the studies of THz surface wave (TSW) has shown a promising future for THz plasmonic devices. The observed enhanced transmission and other effects are in fact due to the interaction between the TSW and the subwavelength metallic structures. Therefore, it is important to be able to physically picture the actual surface wave field pattern on the metal surface and how it could be manipulated. However, the experimental technique to study this fundamental property hasn't yet been available. The characteristics such as absorption and dispersion of surface plasmons in the dielectric coating layer on metal surface have been only studied in theory [34].

The THz wavelength has unique advantages in surface wave studies. First, the conductivities of many metals are large enough in the THz range so that they can be considered as perfect conductors. Consequently, many simplifying approximations can be made without losing accuracy. Second, the wavelength in THz range is short enough so that most quasi-optical devices (such as mirrors, lenses, fibers…) are available with reasonable dimensions for manipulating and guiding of THz beams. Moreover, despite the "loosely bound" property of the THz surface wave due to the high metal conductivity, because of the short wavelength, the spatial extension of THz surface wave is not more than a few centimeters. Thus, a complete picture of the surface wave field decay is much easier to measure compared to microwave range. Third, Grischkowsky's THz antenna receiver makes it possible to measure the broad band THz surface wave field in a quasi-near field scale ($\lambda/12$).

In this study, the experimental technique has been successfully developed and demonstrated. The surface wave is experimentally studied on a smooth (but not polished) metal surface and a dielectric coated metal surface. For both cases, the complete transverse field profile and the propagation parameters such as absorption and dispersion are measured. The effect of field confinement induced by the dielectric coating is demonstrated. The results are favorably compared to the theoretical predictions.

1.3 Scope of this report

In this report, we present our experimental and theoretical studies of the surface waves on both bare and dielectric coated plane metal surfaces.

In Chapter 2, the experimental setup is introduced. The standard THz-TDS system was modified to directly measure the electrical field distribution near the surface with high spatial (25 μm/step) and temporal resolution.

In Chapter 3, the measured time domain signals on bare and dielectric coated metal surface are presented. The results are discussed together with the diffraction effect in the system. Fourier transforms of the time domain signals are performed to view the surface wave field in the frequency domain. The quasi-near field measurements are successfully performed. The observed exponential transverse field decay is in good agreement with the theoretical predictions.

Chapter 4 is focused on theoretical study. For the bare metal surface, the 1/e surface wave extension distance, also called skin-depth, is derived. For the coated sample, instead of using the general electromagnetic wave equation method to analyze the structure [22], we took advantage of the feature of the high THz metal conductivity, by assuming the metal to be perfect conductor. The problem is then simplified and easy to solve using a well-established model, which maintained high precision. The accuracy of the assumption was verified by comparing our results to the non-simplified solution from literature. The dispersion and absorption of the film coating structure are also calculated. The overlap integral method is used for the evaluation of the system coupling. The coupling coefficients, as well as other system parameters, which are responsible for the reshaping of the surface wave pulse, are also calculated and estimated.

In the second part of chapter 4, the theoretical predictions are verified by the experimental results. The observed surface wave field shows the exponential fall-off feature in good agreement with the theory. The input THz reference pulse is used as the input for the numerical simulation of the surface wave propagation process. The calculated output surface wave pulse shows excellent agreement with the experimental measurement.

Chapter 5 and 6 will review the work presented here and draw conclusions about what has been learned. Future work will also be discussed.

Chapter 2 Experimental Setup

The schematic of the experimental setup is shown as the fig. 2-1 below, which shows the complete lay-out of the modified THz-TDS system. Femtosecond laser pulses generated by Ti:Sapphire laser are split into two arms: one goes to the transmitter as the pump pulse

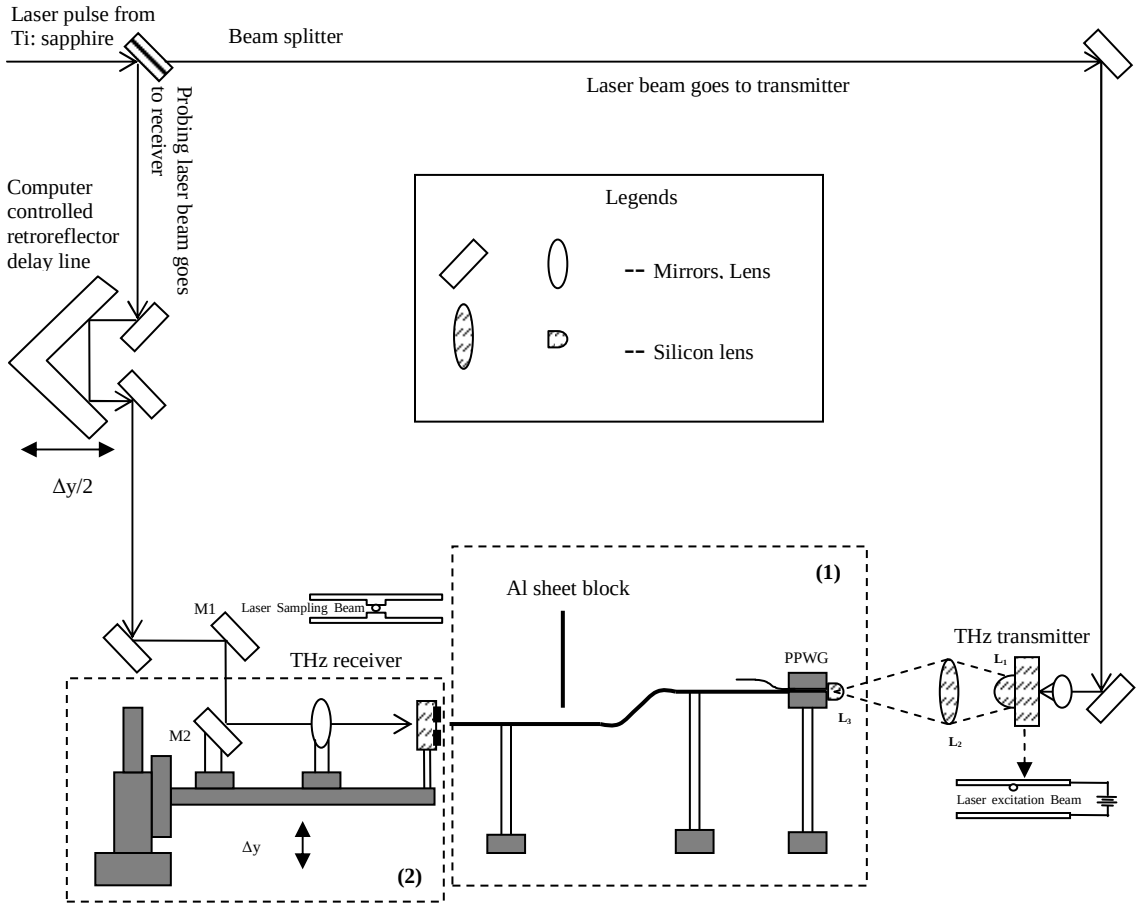

Figure 2-1. 2D schematic of the system setup

and the other goes to the receiver as the probe pulse. At the transmitter side, when the laser pulses are focused onto the transmitter chip, the THz pulses are generated by the transmitter with E field vertically polarized. The generated picosecond THz pulses pass through three silicon lenses L_1, L_2 and L_3 and are focused into the entrance slit of the parallel plate waveguide (PPWG). The plano-cylindrical lens L_3 produces a line focus on the input air gap between the two Al plates of the PPWG, thereby coupling the THz pulses into the waveguide. The PPWG is the starting part of the surface wave apparatus, which is shown in the dashed box 1.

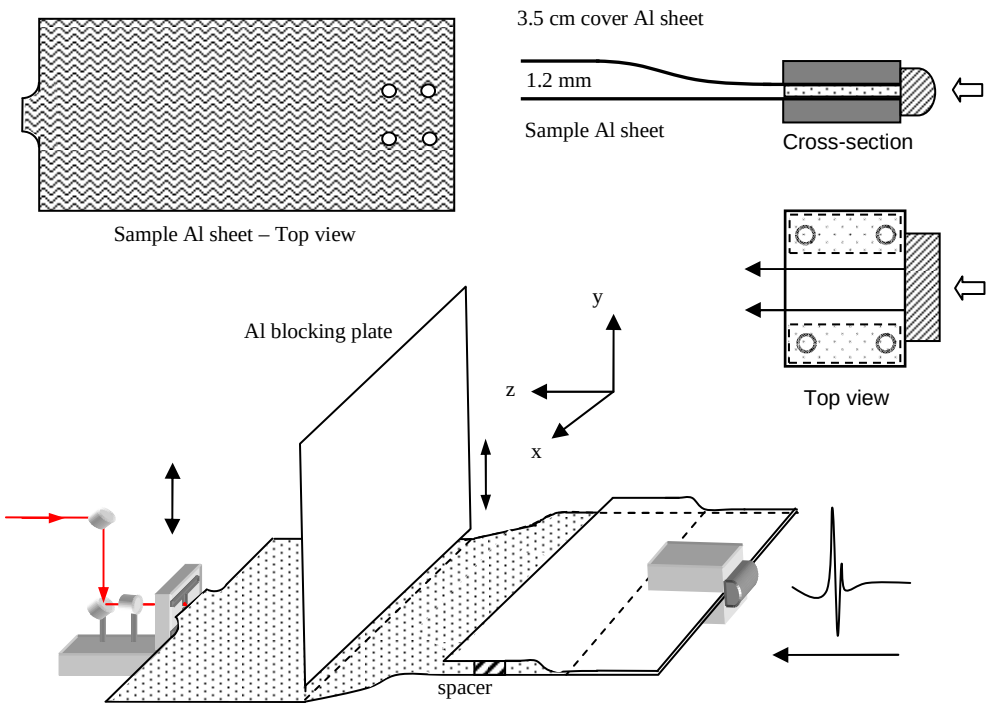

Figure 2-2. 3D schematic of the surface wave apparatus

Fig. 2-2 shows the detail of the surface wave apparatus. The THz surface wave (TSW) propagates on a 24-cm-long by 10-cm-wide by 100-μm-thick sample Al sheet with a bare or dielectric-coated surface. As shown in the upper right in fig. 2-2. An extension of the

Al sheet is placed into the PPWG on top of the lower plate of the PPWG to couple the THz wave onto the Al sheet. On top of the sample Al sheet, there is another piece of 3.5 cm long Al sheet with 100 μm separation from the bottom sheet to form the actual parallel plate structure. The TSW launching part is the aperture outside the left of the PPWG, the two waveguide sheets make a 1.2 mm slowly opening flare aperture structure to realize the excitation of the surface wave. This launching configuration is similar to the earlier Zenneck wave setup [26], however, the newly added 3.5 cm long flexible cover sheet forms an adiabatic flare opening, which provides better bandwidth coupling efficiency [35].

It has been theoretically proven that no surface wave launcher can provide a 100% conversion of the incident power into surface wave power [6]. Therefore, along with the surface wave, there is always a freely propagating THz wave coming out from the flare. To eliminate the effect of this part in the received signals, a 3.5 mm-deep adiabatic curve is intentionally made to the Al sheet in order to create a different propagation path for the two parts of waves. Then a 10 cm wide Al plate is vertically placed in front of the curve with 3 mm opening below the edge of the plate at the downstream of the curved surface. The distance from the blocking plate to the end tip of the Al sheet is 8 cm. However, it is impossible to completely block the freely propagating wave because diffraction occurs when the freely propagating wave is passing through the slit. More detailed discussion will be in Chapter 3.

The receiver is located at the end of the sheet to detect the linearly polarized TSW field that is perpendicular to the sheet surface, as shown in the fig. 2-3. The receiver is fabricated on a double side polished silicon-on-sapphire (SOS) wafer so that the laser sampling beam can penetrate the sapphire substrate and irradiate the semiconductor between the antennas. To enable the direct measurement of the electrical field, the receiver is modified from the standard THz-TDS system. There is no silicon lens attached to the receiver chip and no second identical large convex silicon lens in front of the receiver to focus the incoming THz wave from the L_2. Thus the mirror symmetry of the system, which is a required condition for 100% energy transfer, is compromised. Without the silicon lens in between, the metal antenna side is closely placed to the edge of the sheet (distance less than 30 μm) to allow a direct detection of the THz electrical field. As shown in dashed box 2 in fig. 2-1, a periscope configuration is used to enable the vertical movement of the receiver. The receiver and two optics (M2 and optical lens) are mounted on a breadboard so that they can move vertically to measure the TSW field at different heights relative to the surface. The movement of the breadboard is controlled by a micrometer knob whose minimum measurable distance is 1/1000 inch (≈ 25.4 μm).

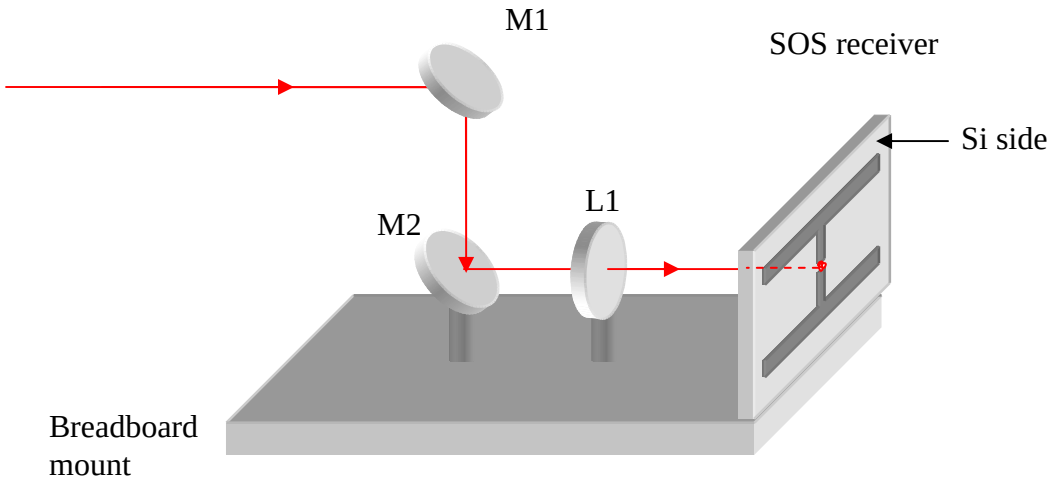

Figure 2-3. The optical part of the receiver

Two samples are prepared for the study. They are made of two identically sized (24 cm×10 cm×100 μm) Al sheets. For sample 1 the Al sheet is directly used with its original bare surface; for sample 2 the Al sheet surface is coated with 12.5 μm polyethylene film. The refractive index of the film is assumed to be constant n = 1.5 in the frequency range of interest.

Similar to the standard THz-TDS system, on the receiver side, there is an optical delay line made up of a computer controlled motorized retroreflector. The movement of the retroreflector can change the laser path length at the receiver side and consequently change the timing of the photo-conductive switched receiver. The experiments were performed in this way: first, the receiver is moved to a pre-selected position. Then, the system starts to take data by controlling the delay line to scan through a long enough distance (8 mm ~ 10 mm). Scans are repeated as the receiver is moved to different positions.

During the experiment, the receiver changes its position upward or downward as shown in fig. 2-1. The movement of the receiver mount will change the distance between two mirrors (M1 and M2) and consequently change the optical path length of the receiver side as well. For example, if the receiver is moved upward, the distance between M1 and M2 will become smaller. Then the total optical path length on the receiver side will be smaller. This will make the probe laser pulse arrive the receiver earlier. However, the arrival time of the THz surface wave pulse remain unchanged. Therefore, the motorized delay line needs to scan further to compensate the shortened optical path and consequently the detected signal pulse appears later in time, compared with before moving the receiver upward. Therefore, when studying the arrival timing of the received surface wave signal, the path length change induced by the movement of receiver should to be considered and compensated.

Scanning range and step sizes

The system allows the maximum receiver scanning from 3 mm below the surface to 22 mm above the surface. But the scanning range for most experiments and being compared as a common range is from 1.65 mm below surface to 1.14 mm above surface, which is called a **complete set of data.** Small step sizes (25 μm and 50 μm) were used in the range of -0.5 mm to +0.5 mm from surface, and bigger step sizes (125 μm and 250 μm) were used for the other positions.

Chapter 3 Experimental Results and Discussions

3.1 Individual Signal

The reference THz pulse in fig. 3-1 is taken with the surface wave apparatus out of the system. The optical arrangement for the reference pulse is shown in fig. 2-1 and the schematic diagram in fig. 3-1.

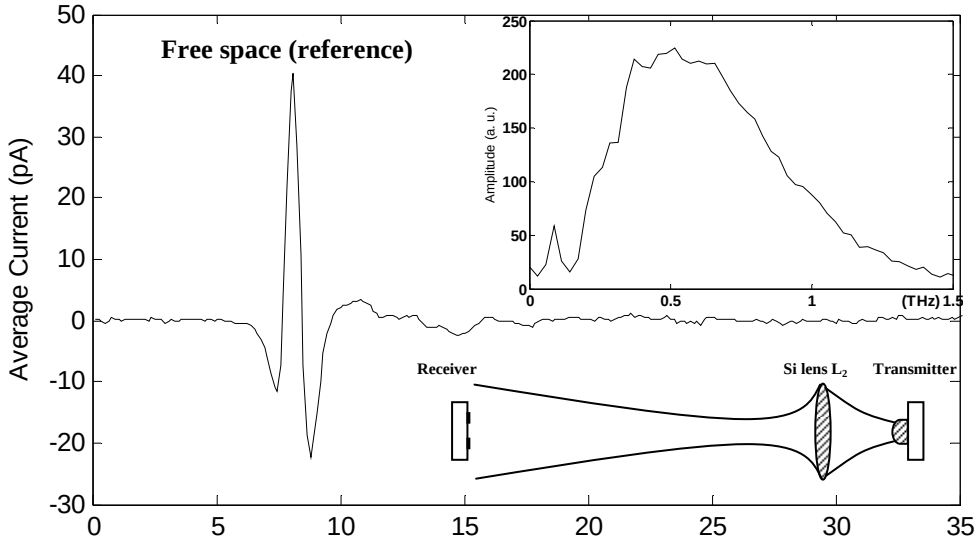

Figure 3-1 Reference signal

The focal length of the large convex silicon lens L_2 is 15 cm and the receiver is located about 40 cm left to the L_2. The lens L_2 collects the collimated THz beam from the

transmitter located at the right focal plane of L_2. L_2 focuses the THz beam into a frequency dependent spot at the left focal plane with beam radius proportional to the wavelength. For example, the spot size for 0.5 THz is approximately 20 mm diameter and spot size for 1 THz is around 9 mm. Then, the THz beam continues propagating freely 25

cm illuminating the receiver with a much bigger frequency dependent THz beam spot, for example, 25 mm for 0.5 THz and 16 mm for 1 THz. As shown in fig. 3-1, both the bandwidth and amplitude are smaller than those obtained with the standard THz-TDS systems [36].

3.1-1 Signals on bare metal surface

As introduced in Chapter 2, sample 1 is a 24 cm long, 10 cm wide and 100 μm thick, bare aluminum sheet; sample 2 is a sheet of the same dimensions, but with a 12.5 μm polyethylene film coating. The measurements of samples can be carried out by taking multiple scans with different vertical positions of the receiver from below to above the surface. Fig. 3-2 (a), (b) and Fig. 3-4 are the THz surface wave signals of sample 1 and 2 taken at the level of surface. The corresponding amplitude spectra are plotted in the inset.

Fig. 3-2 (a) is taken on sample 1, the bare surface without the blocking plate. From the structure of the coupling mechanism, it is obvious that the received signal is a mixture of the surface guided wave and the unguided freely propagating wave because the system structure allows the collinear propagation of both waves. The coupled and uncoupled THz waves come out together from the flare opening of the PPWG. The surface wave

coupling occurs during its entire propagation, and the coupled surface wave propagates along the adiabatically curved surface. The freely propagating wave comes out from the 1.2 mm flare opening of the PPWG and radiates into free space the surface as a diffracted wave which keeps spreading as it propagates.

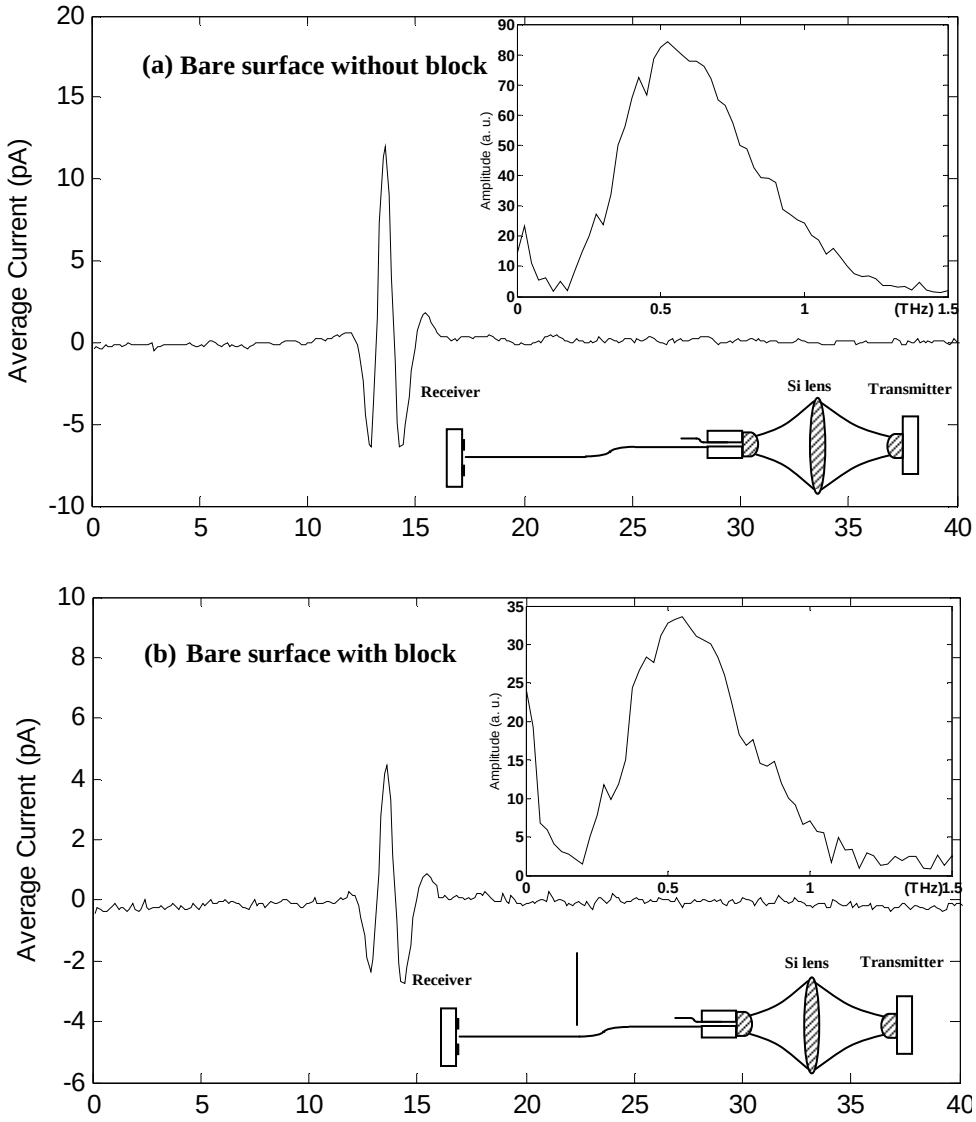

Figure 3-2. (a) Surface wave pulse on bare metal surface, no block (b) Surface wave pulse on bare metal surface with block.

With the blocking plate with a 3 mm opening perpendicular the surface, as the case of fig. 3-2 (b), the signal amplitude is greatly reduced. This is believed due to blocking the

majority of the diffracted wave from the flare. However, the reduced signal arrives at the same time as the unblocked one. This indicates that the received signal still contains wave that comes along the path of the freely propagating waves. This shows that the unguided free space waves again "find" their way to overcome the obstacles under the help of diffraction and propagate to the receiver. The surface wave in the signal, although is weak, can also be identified and will be shown in the later data processing.

On the bare metal surface, diffraction has a significant contribution to the signal. So it is necessary to assess diffraction from the waveguide flare and the slit of the blocking plate in more detail. To simplify the problem, the metal sheet is assumed to be a straight plane with no curvature. When there is no blocking plate, the only diffraction is from the 1.2 mm wide flare opening of the waveguide, equivalent to single slit diffraction with a conducting sheet extending in the propagation direction from one edge of the slit. The diffracted wave from the flare opening propagates 20 cm to the receiver without disturbance. Because of the Al sheet's mirror effect, the equivalent diffraction slit width should be doubled to 2.4 mm, and the Al sheet is the centered symmetric plane. Here, the Fresnel number $F = a^2/(L\lambda)$, where a is 1.2 mm, the half width of the slit, L = 200 mm is the propagation distance and λ is the wavelength. At λ = 600 μm, corresponding to 0.5 THz, F = 0.012 <<1, so it can be considered to be far field diffraction. The far-field half-space amplitude diffraction pattern of a single slit is described as a $(sin\theta)/\theta$ function with the central maxima at the metal surface. Assuming the central peak signal amplitude taken without blocking plate to be 1, the area defined by the intensity diffraction pattern stands for the total power from the 1.2 mm slit.

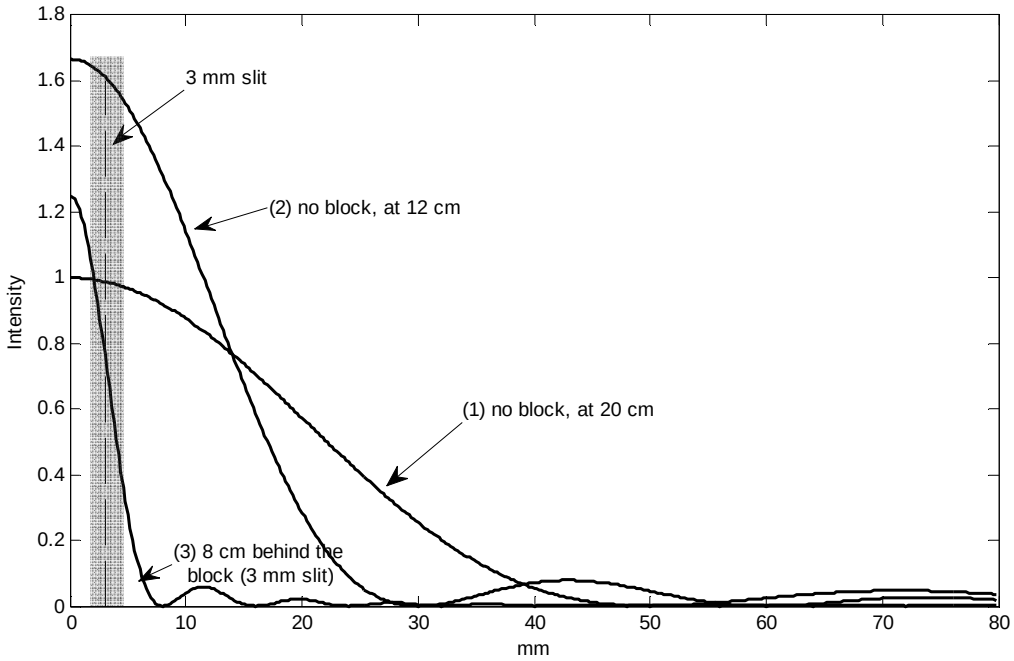

Figure 3-3. The intensity diffraction pattern for 0.5 THz, λ = 600 μm: (1). The 1.2 mm flare opening without block, (2) the 1.2 mm flare opening at the blocking plate, (3) the 3 mm slit of the blocking plate

In fig. 3-3, curve 1 shows the power diffraction pattern from the flare opening at the receiver plane. When the blocking plate is inserted at 8 cm from the receiver, corresponding to 12 cm from the flare opening, the free space waves diffract 12 cm from the flare opening and arrive at plane of the 3 mm slit between the plate and metal sheet. The slit truncates the diffraction pattern to 3 mm; the transmitted wave from the 3 mm aperture diffracts again as it propagates to the receiver. Curve 2 in fig. 3-3 shows the diffraction pattern at the blocking plate — it contains the same amount of power as curve 1. Then the transmitted power through the 3 mm slit (the shadowed area) is diffracted to the receiver 8 cm downstream shown as curve 3, whose area is equal to the shadowed area. Therefore, according to the calculation conserving the total power, when inserting

the blocking plate, the peak amplitude at the receiver should change to 1.25 of the unblocked signal.

In the actual experimental setup, more processes occur besides the diffraction. The surface wave coupling and decoupling occurs along the entire sample surface. The adiabatic curve of the sheet interferes with the free space diffraction. The blocking plate introduces not only the diffraction but also the decoupling of the surface wave. As a result, the experimental data in fig. 3-2 clearly show that the received signal has much more reduction when the blocking plate is inserted in the system, than predicted in the simple calculation above.

The surface wave launching/coupling efficiency is determined by the overlap integral of the excitation field (the diffracted wave field) and the surface wave field [6]. A well-known fact is that THz surface wave (TSW) is weakly coupled to the bare metal surface due to the high metal conductivity, resulting in the TSW exponential fall-off field extending transversely from a few tens to hundreds of millimeters above the metal surface, as shown in Table 1-1. Therefore at the 1.2 mm flare opening of the PPWG, the coupling to surface wave is very low because of the small overlap integral of the two field patterns. As the propagation distance increases, the diffracted $(sin\theta)/\theta$ pattern expands whereas the exponential surface wave field pattern remains the same, because it is the single mode solution determined by the constant metal conductivity. The coupling of the two fields increases at first as the diffracted wave field is expanding closer to the extent of the TSW field giving a larger overlap integral. The diffraction field pattern

keeps expanding and becomes much larger than the TSW field pattern, then the coupling decreases as the two fields are becoming less overlapping. Fig. 3-4 below shows the overlap integral at different distances for 0.5 THz. From the figure, 175 cm gives the optimal coupling.

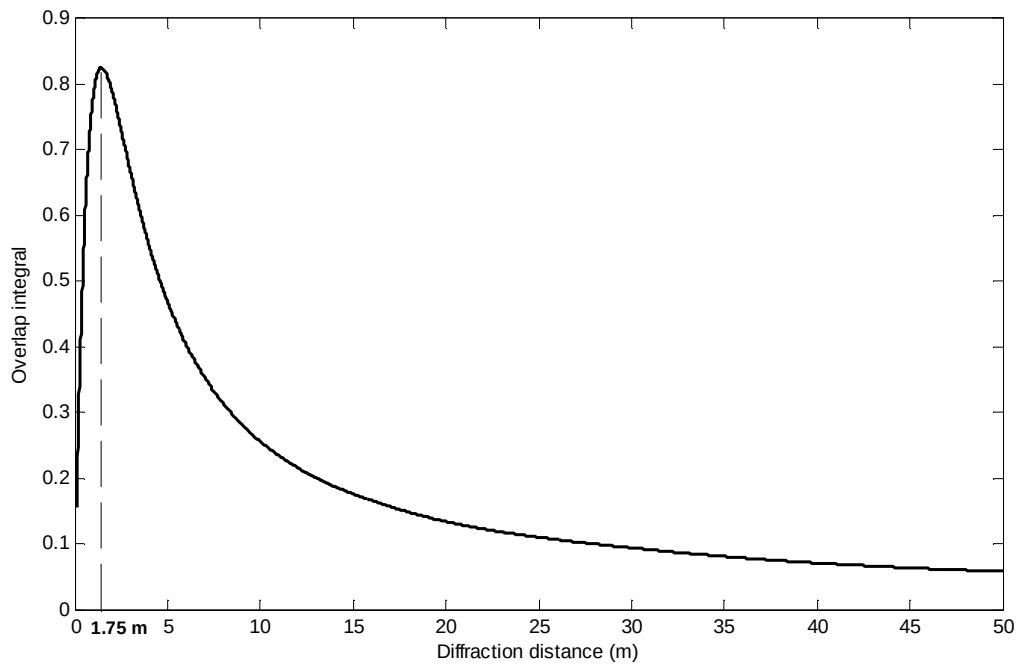

Figure 3-4. Overlap integral of the surface wave field pattern and the diffraction pattern at different distances

Fig. 3-5 below shows the transverse intensity and field profile at a few selected distances. For λ = 600 μm on an aluminum surface, the TSW field pattern is constant and is shown as the dotted line, with 1/e amplitude value of 160 mm. The diffraction patterns at 80 cm, 175 cm and 500 cm and 5000 cm from the flare opening are plotted as solid lines. At 80 cm, the two fields are normalized for comparison. At 175 cm, the overlap integral between the free space diffraction and the surface wave has the maximum value of 0.825, as the two patterns have their most overlapping shapes. Furthermore, for a propagation distance of 500 cm and finally at 50 m, the spatial extension of the two waves have

become so different that they are considered to be well separated and no longer coupled. Therefore, in the measurement on sample 1 with only 20 cm propagation distance, the signal actually contains only a small portion of surface wave while the majority remains

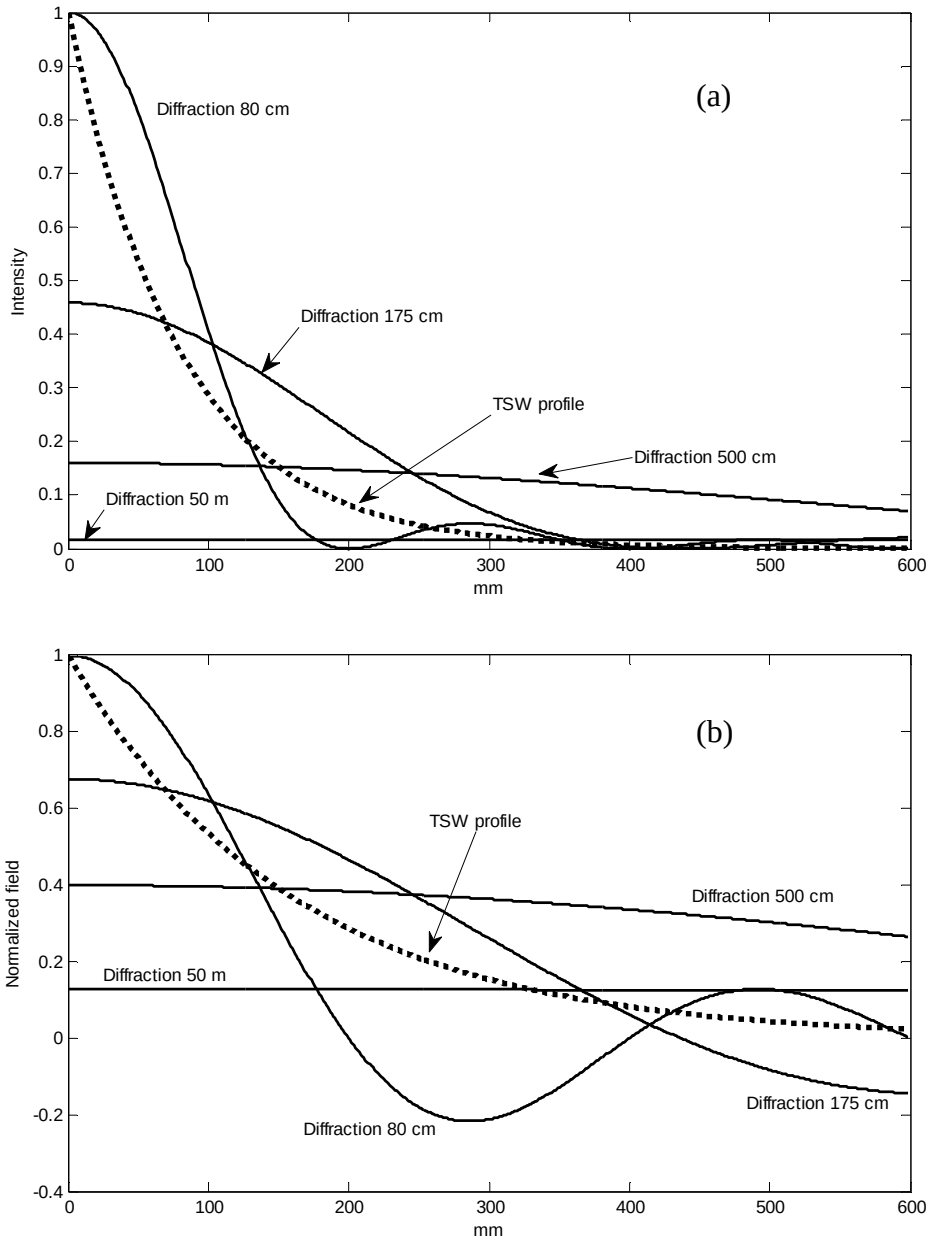

Figure 3-5. Overlapping of the surface wave field pattern (dashed line) and the diffraction pattern (solid line). (a) Intensity. (b) Amplitude.

as the uncoupled freely propagating wave. The TSW is predicted to propagate 137 m before the intensity drops by 1/e. For this distance the 1/e extent of the diffracted wave amplitude is 2800 cm, compared to the unchanging extent of the TSW with a 1/e amplitude extent of 16 cm. In summary, an optimum long (>1000λ) distance is a desired condition for the best coupling of surface waves, however it is impossible to obtain a pure surface wave signal since there is no 100% overlap integral throughout the entire surface. An important point is that the two waves propagate with the same phase velocity to 1 part in 10^8. Consequently, for $\lambda = 600$ μm, the coherence length for energy exchange between the two waves is the stunning value of $10^8\lambda = 60$ km, which raises the question as to whether or not these waves can ever be completely decoupled.

More loss is introduced with the blocking plate in the system. The large spatial extension of the THz surface wave results in a large portion of the wave energy getting truncated by the blocking plate. Moreover, the 3 mm slit opening of below the blocking plate is simultaneously an aperture decoupler which couples the surface wave back into the free space.

Although there is predicted radiation loss of the surface wave at the surface bending [11], it believed to be an insignificant loss factor in this experiment because not much energy is actually coupled into the surface wave. However, the surface bending is responsible for the signal reduction because it creates an indirect path for the diffracted wave from the PPWG flare opening so that even less energy finally gets its way through the slit. Therefore, the measured surface wave after the blocking plate is lower in amplitude.

3.1-2 Signals on dielectric coated surface

In the measurement of sample 2, as shown below in fig. 3-6, the presence of the dielectric coating greatly compresses the spatial extension of surface wave and consequently greatly improves the surface wave coupling. Therefore, the signal is much stronger. The dielectric coating confines the surface wave field to within only a few wavelengths from the surface so that the wave can pass through the slit and arrive at the receiver. The signal of sample 2 also shows that the pulse has been stretched to 25 ps long with a positive chirping feature, where high frequencies arrive latter in time. This is also evidence that the dielectric film is guiding the wave with dispersion. The relative smooth spectrum of the signal shows no sharp low-frequency cut-off or any unusual oscillations, indicating single TM_0 mode propagation in the dielectric with zero cutoff frequency.

Compared with the reference spectrum, the amplitude spectrum of frequency from 0.5 ~ 0.7 THz of film-coated surface wave is higher than the reference. The first reason is that the free space signal has low transfer efficiency as mentioned at the beginning of this chapter. However, the surface wave apparatus has a confocal Si lenses arrangement which provides better coupling from the free space into the waveguide system. The second reason is the surface waves on the dielectric coated surface propagate in more tightly guided mode so that more energy is preserved during the propagation.

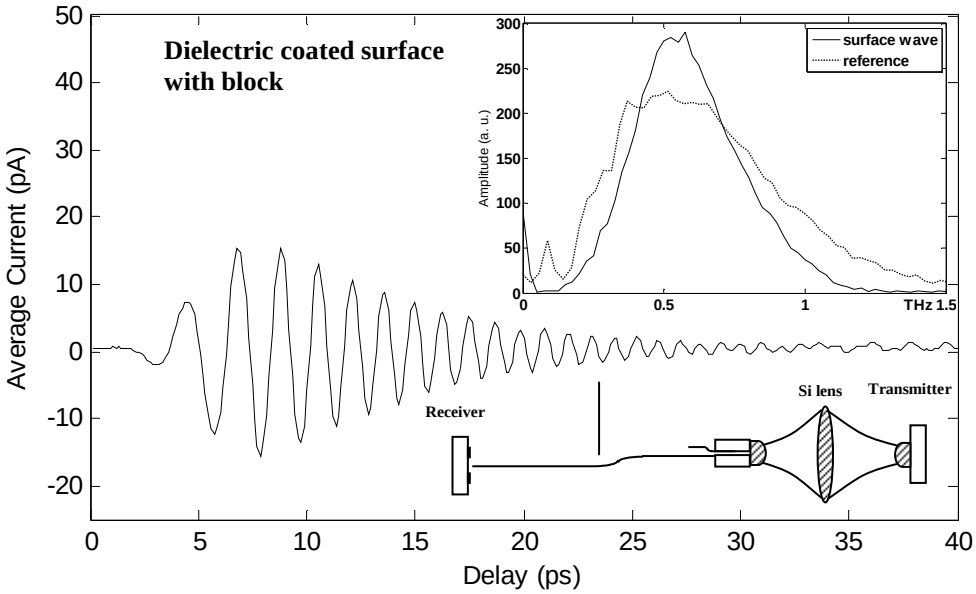

Figure 3-6 THz surface wave pulse on dielectric coated surface with block

On the coated surface, diffraction is no longer the dominant effect in the received signals compared to the case of bare metal surface. The comparison is made in the fig. 3-7, the top curve (a) is the signal taken without block, and the middle curve (b) is taken with the blocking plate. It shows when the blocking plate is inserted, no major change happens to the signal as it does on the bare metal surface. This indicates that with the improved coupling due to the dielectric film, more energy is being carried by the surface wave mode and propagates closely along the surface, whereby the blocking plate can have very limited influence. The unguided freely propagating part of the wave that can be blocked or diffracted can be obtained by subtraction of the curve in (b) from the curve in (a). As shown in (c), the freely propagating wave is the small leading part of the signal which propagated along the shorter straight line path.

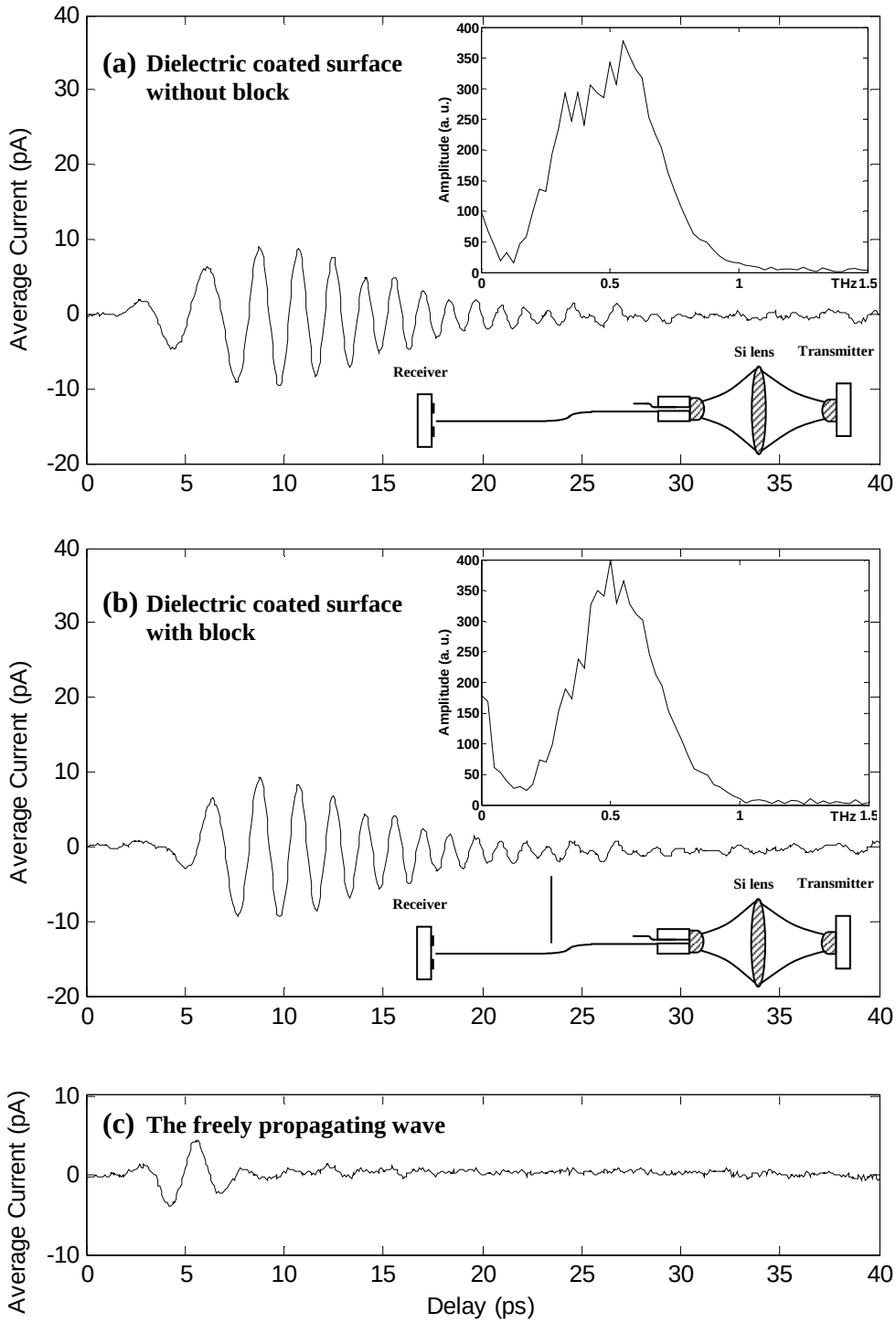

Figure 3-7. TSW pulse on coated surface without block. (b) TSW pulse on coated surface with block (c) The freely propagating wave given by subtraction of TSW pulse (b) from TSW pulse (a). Inserts show corresponding spectra

3.2 Signals taken above surface

Signals at different heights above the surface are measured by moving the receiver. As introduced in the fig. 2-1, the time delay effect of the movement of the receiver has to be compensated to indicate the actual arrival time of each signal before presenting the THz signals in time domain. For example, in the fig. 3-8 (a), the lower curve was taken at the surface and the upper curve was taken 0.60 mm above the surface. From the figure it can be seen that there is an apparent time delay between the two signals. As shown in fig. 2-1, when the receiver is moved upward by 0.60 mm, then the distance between M1 and M2 becomes shorter by 0.60 mm, and therefore the optical sampling pulse will arrive the receiver 0.60 mm/c = 2.00 ps earlier. However, the arrival timing of the THz pulse signal remains the same. Therefore in order to measure the signal, the sampling pulse will need to “wait” 2.00 ps longer to be synchronized with the surface measurement and so the time delay is created. Therefore, in order to compensate for this time delay, the signal above the surface needs to be moved to 2.00 ps earlier in time (to the left) relative to the signal on the surface, as shown in fig. 3-8 (b).

The fig. 3-8 (b) shows that after removing the effect of position change of the receiver, the peaks in the surface wave pulse at 0.6 mm above the surface are aligned precisely with the corresponding ones in the pulse on the surface except for their smaller amplitudes. This indicates that the signal above the surface actually arrives at the same time as the one on the surface which is expected according to the plane wave mode profile, because the entire wavefront propagates with the same velocity.

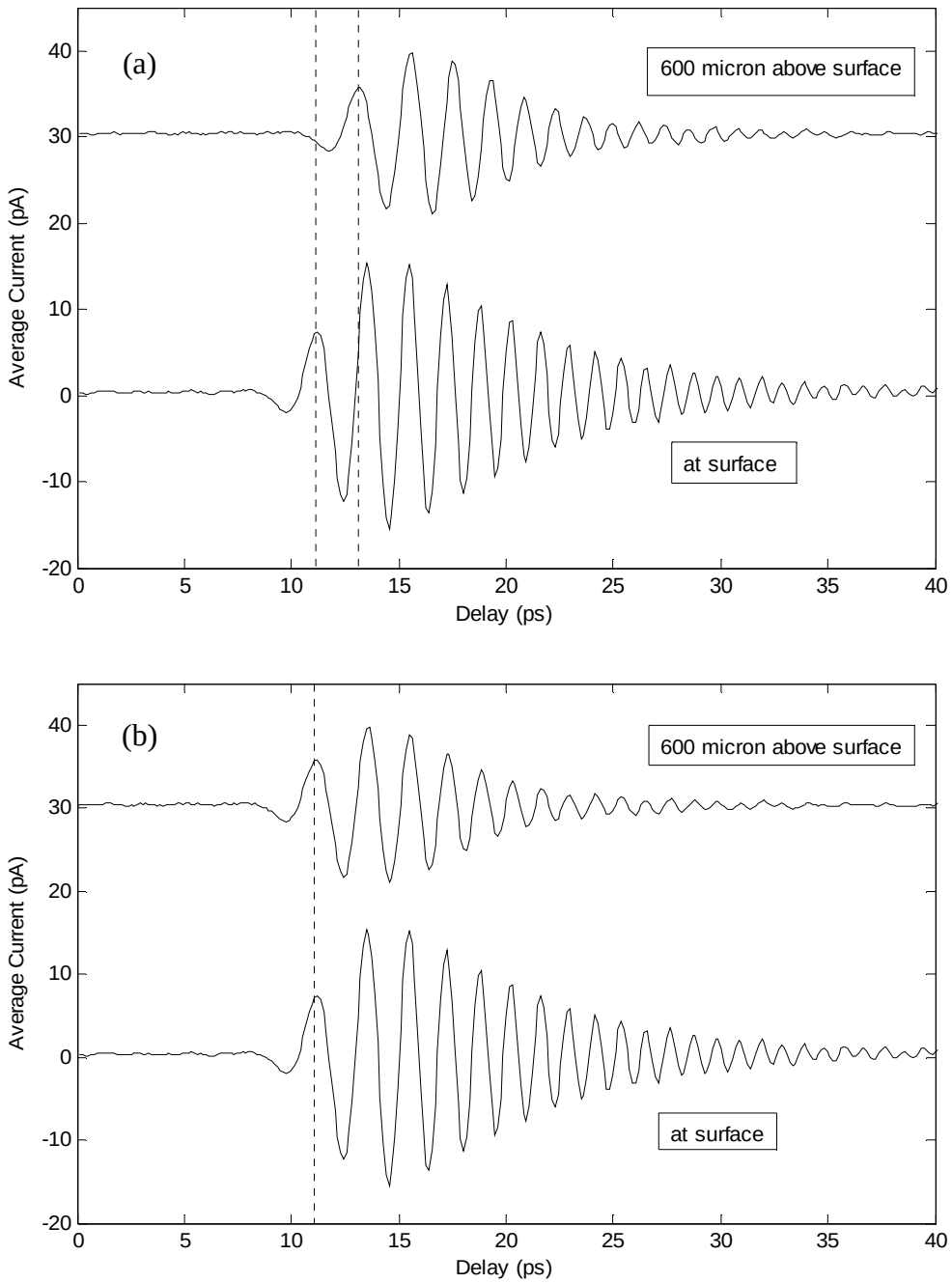

Figure 3-8. THz surface wave pulses measured at the surface and at 0.6 mm above surface (a) before compensating the time delay caused by receiver movement. (b) after compensation

As the receiver moves above the surface, the signal amplitudes of both sample 1 and sample 2 decrease. The dielectric film covered sample 2 exhibits stronger confinement of

the surface wave than the bare surface and hence results in a faster fall-off of the surface wave field. Fig. 3-9 shows the comparison of signals measured at the surface and above

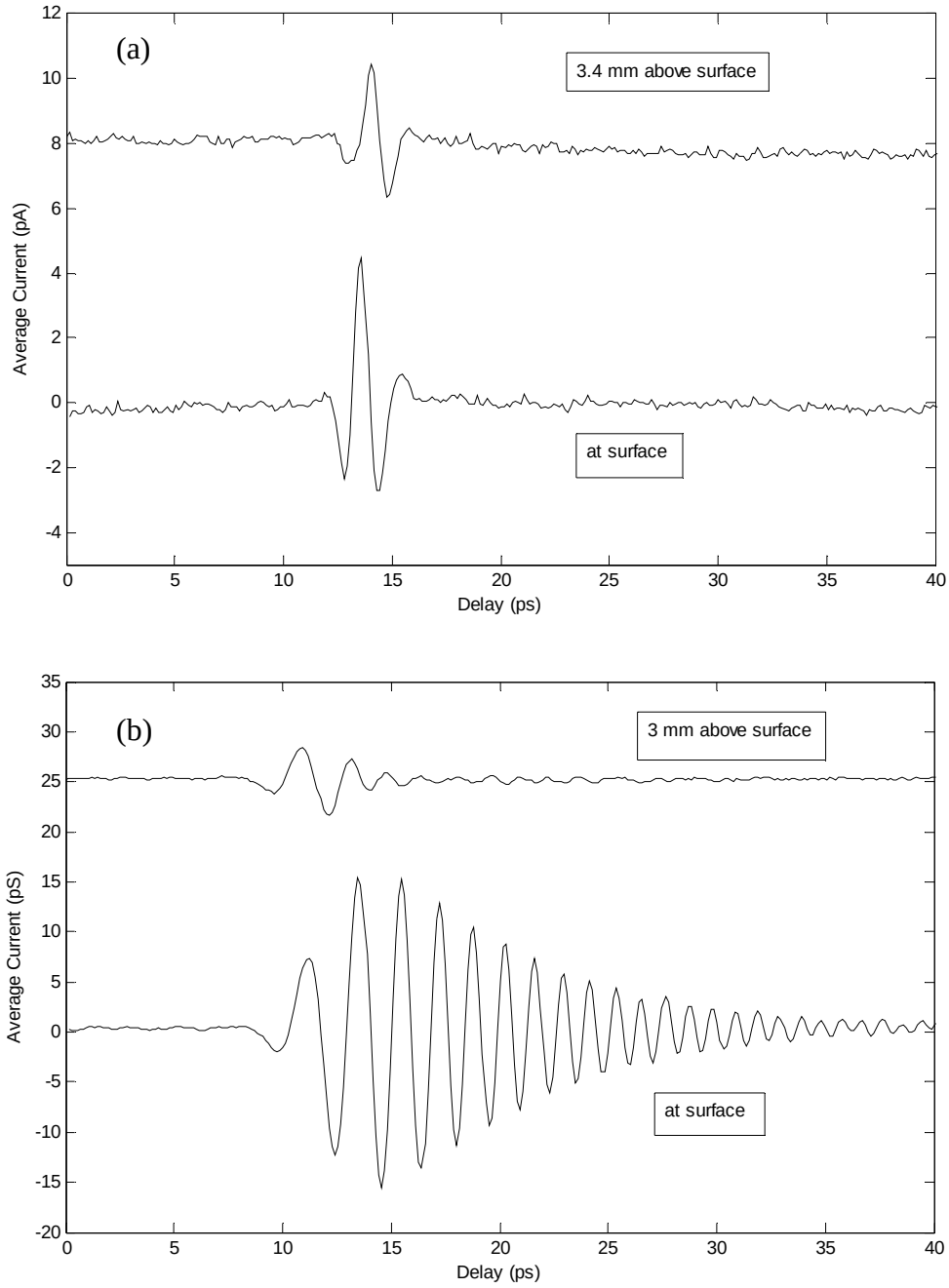

Figure 3-9. Comparison of signals measured at the surface and above surface (a) bare surface – sample 1 with block. (b) dielectric coated surface – sample 2 with block

the surface. In fig. 3-9 (a), for the bare surface - sample 1, the upper curve is measured at 3.4 mm above the surface, the amplitude drops 50% of the lower curve at the surface,. For sample 2, shown in fig. 3-9 (b), when the Al surface is coated with a 12.5 μm dielectric (n = 1.5), the field extension of the surface wave is greatly compressed. At 3 mm above the dielectric-coated surface, the amplitude drops to 20% of the surface signal.

As the receiver keeps moving, more signals are taken, a clear trend of TSW field fall-off is observed. In below fig. 3-10, the time domain signals are plotted according to their corresponding receiver positions. It clearly shows a snapshot of the entire surface wave, and gives the field fall-off profile above the surface. Because all the time shifts have been compensated, in fig. 3-10, the displayed relative positions of the waveforms in time

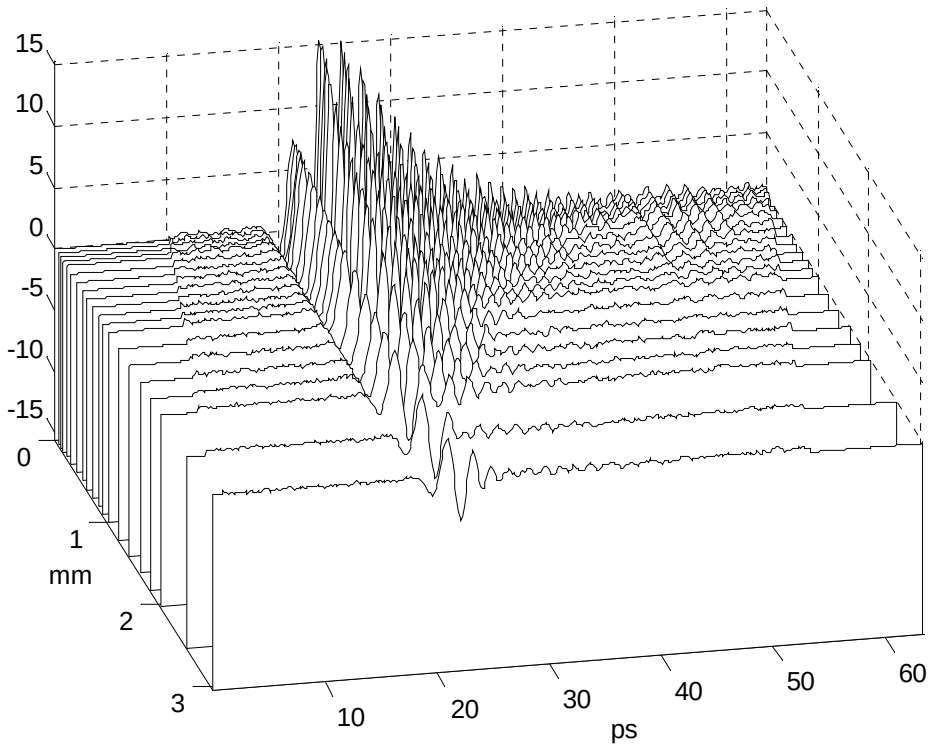

Figure 3-10. The time domain surface waveforms above dielectric-coated surface with block.

reflect their actual arrival timing. This again shows that the THz surface waves at different height above the surface hit the receiver at the same time. It is also worth noticing that in the fig. 3-10, the long ringing tail of high frequency components fade away, as the wave extends higher into the space. The frequency dependency of the fringing field fall-off is again a nature of the guided surface wave, which is better presented in frequency domain.

Fourier Transforms are performed on all the above time domain signals so that the amplitude spectra of the signals taken at different receiver positions are obtained. By putting the spectra together in the order of their corresponding receiver positions, the amplitude fall off of the surface wave can be compared in frequency domain. Fig. 3-11 shows the spectra from surface to 6 mm above the bare metal surface without blocking plate.

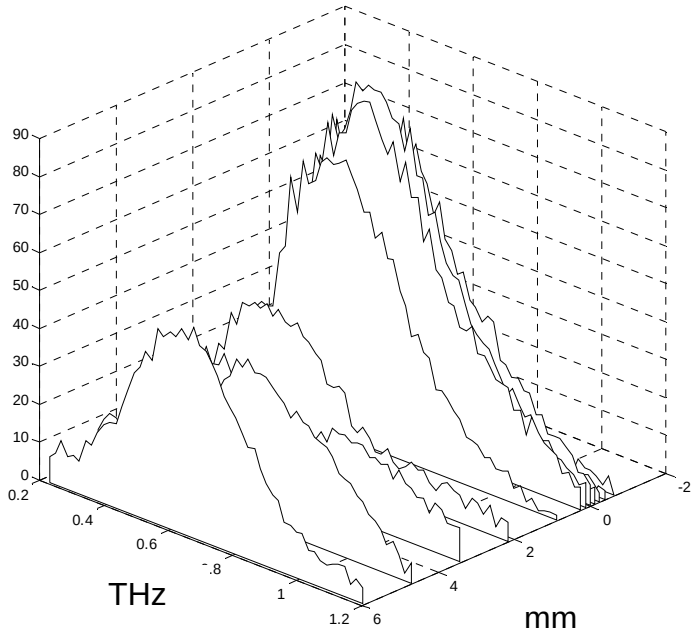

Figure 3-11. Amplitude fall-off viewed in frequency domain

Therefore, for each individual frequency, by picking out the amplitude points at all positions from the spectra in fig. 3-11, a spatial amplitude fall-off distribution can be obtained, as shown in fig. 3-12

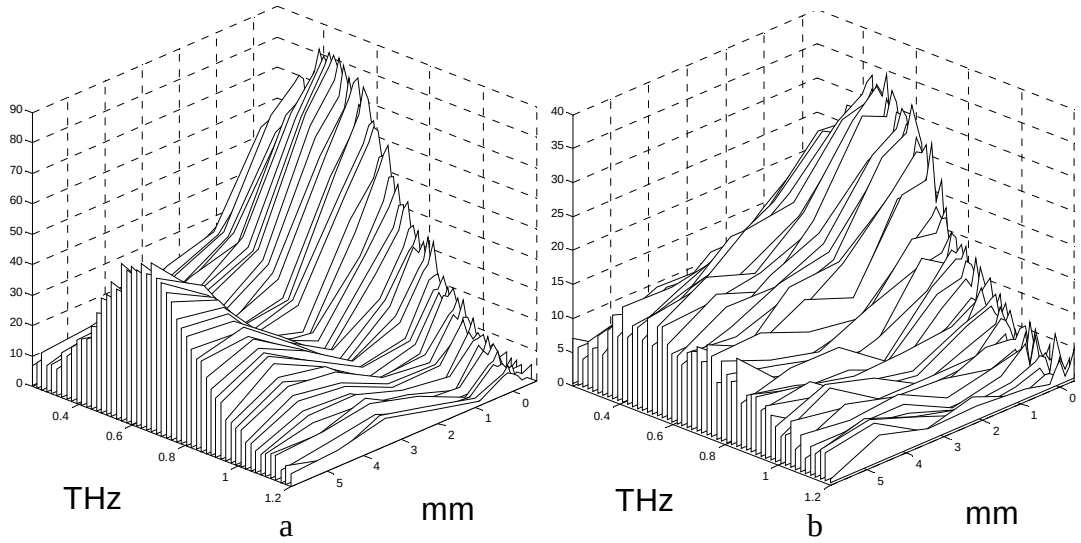

Figure 3-12. unnormallized frequency dependent field fall off curves: a- bare metal surface without block, b- bare metal surface with block

Because the amplitude has its maximum value at the surface, all the amplitudes are usually normalized to the amplitude at the surface to show a clearer comparison. The normalized amplitude fall-off curves for each individual frequency from 0.2 to 1.2 THz are plotted fig. 3-13 (a) for bare metal without block, (b) for bare metal with block. Fig. 3-13 (a) and (b) show the experimental results of the frequency dependent field distribution on the bare metal surface without and with blocking plate, respectively. Both of the two situations show that the detected surface wave field has maximum strength at the surface, and then the field decreases with the increase of the distance from the surface. The field strength increases when the distance is greater than certain value,

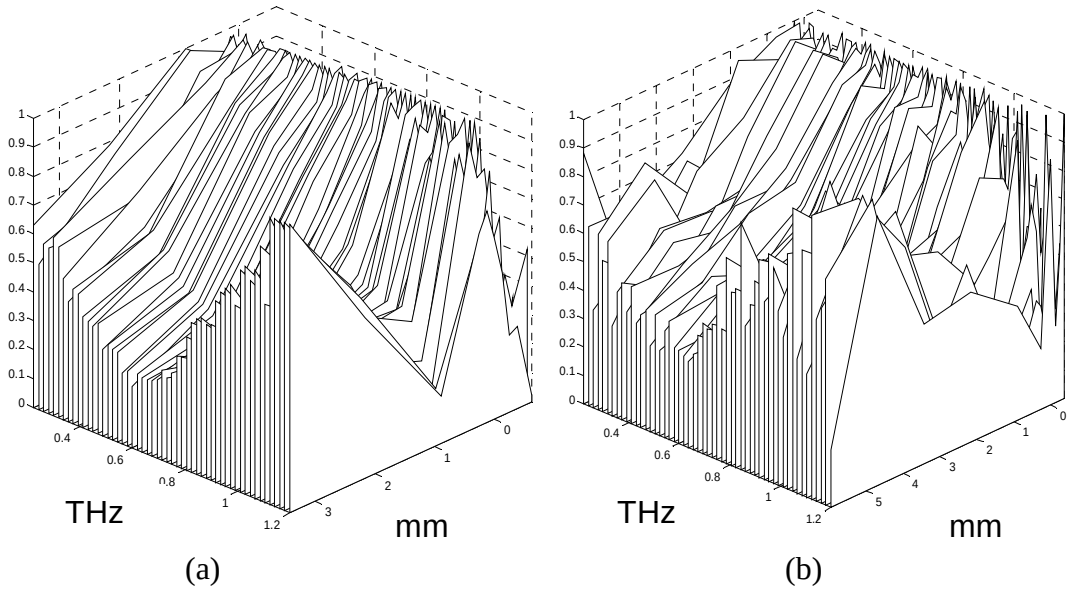

Figure 3-13. Experimental surface wave fall-off (a) bare surface without block. (b) bare surface with block

however for some lower frequencies the increase happens outside of the margin of the figure for it takes longer distance. Both the decrease and increase are frequency dependent. The field distribution with the blocking plate has poor signal to noise ratio which causes the trend less obvious.

As discussed earlier, both surface wave coupling and free space diffraction occur to the bare metal surface case. Therefore, the theoretical field distributions of these two effects are worked out and plotted. Fig. 3-14 (a) is the surface wave field fall-off on aluminum surface. High metal conductivity in THz results in loosely bound surface wave field, therefore the fields are hanging far away above the surface and show a slow fall-off curve. Fig. 3-14 (c) is the far field diffraction pattern of the waveguide flare opening which corresponds to the unblocked case. After diffracting 20 cm away from the flare opening, the diffraction pattern is widely spread across the vertical plane and also results

in almost flat field distribution within 4 mm from the surface. Fig. 3-14 (d) is the diffraction pattern of the 3 mm slit of the blocking plate which corresponds to the case with block, short distance and wider slit width results in narrower first order diffraction peaks, especially at frequency higher than 1 THz, the second order diffraction peaks even show up.

The bare metal surface case is a combination of weakly bound surface wave and strong free space diffraction, therefore both features of surface wave and diffraction can be found in the experimental field patterns. In the case of bare surface without blocking plate as shown in fig. 3-13 (a), the field decrease from the surface maximum shows that there is coupled surface wave existing in the signal. The field increase at some distance from surface is believed to be due to the diffraction. Also, because the wave has long propagation length on the surface, the diffracted wave expands closer to the surface wave pattern, which is, the surface wave field pattern fig 3-14 (a) has similar distribution as the far field diffraction of the flare opening fig. 3-14 (c). Therefore, the condition does allow a better surface wave launching which is confirmed in the fig. 3-13 (a). Due to the same reason, when blocking plate is inserted, the launching condition is worsen and results in lower signal amplitude. The field pattern before normalization below clearly shows the change.

Comparing with the theoretical fall-off curve of bare Al surface of fig.3-14 (a), the actual field falls much faster than the theoretical prediction. This discrepancy is not surprising because it has been observed and reported by many earlier researchers [13, 22, 23, 27,

37-40]. T. Jeon of our group had the similar observation [26]. According to the theory, surface waves are modeled on ideal flat metal surface. So in experiment, extremely optically smooth and flat surface is needed to satisfy the theoretical prediction of large spatial field extension. Surface roughness of the sample Al sheet also increases the

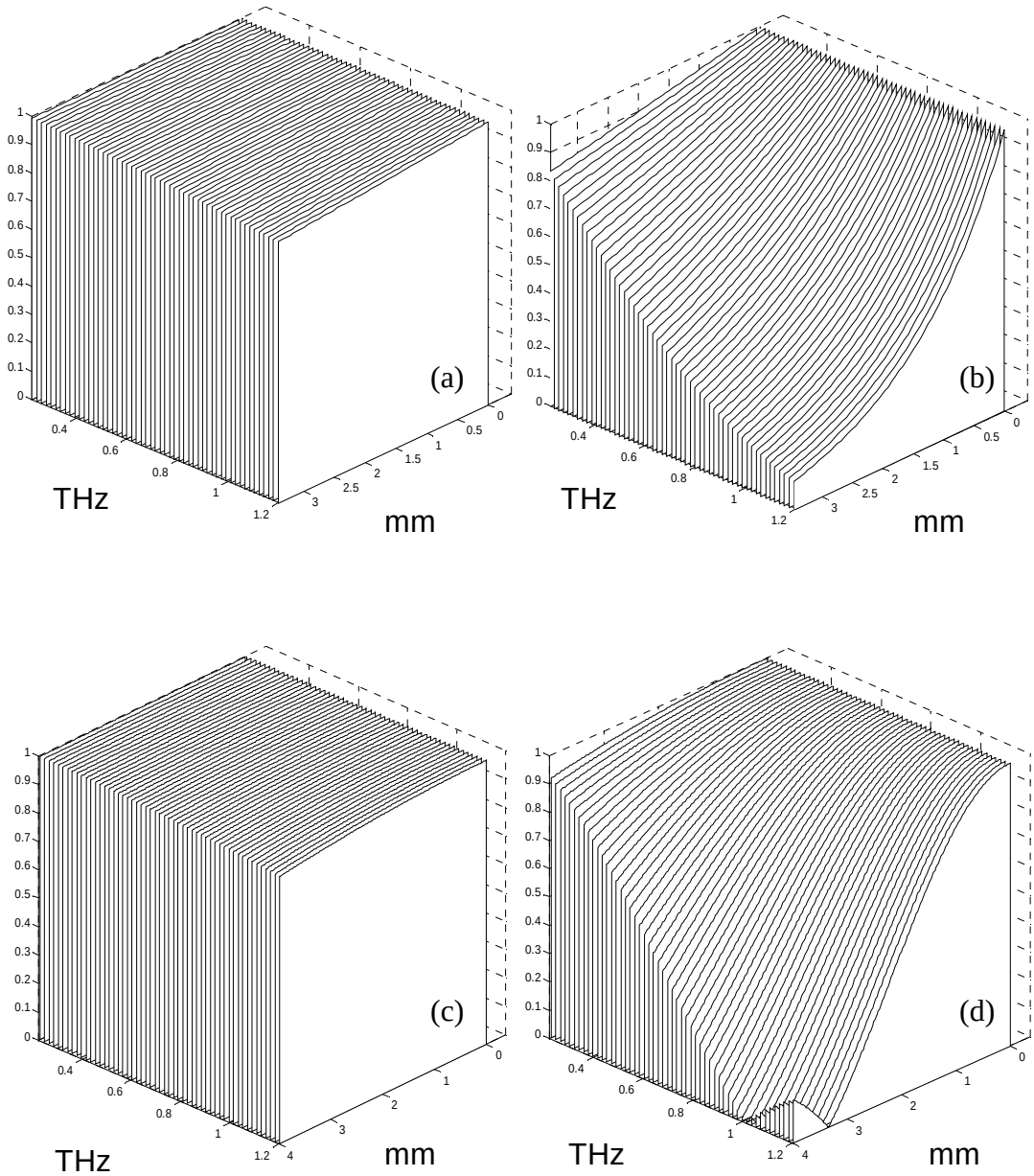

Figure 3-14. (a) Theoretical fall off on bare surface. (b)Theoretical fall off reduced with a factor of 28. (c) Diffraction pattern from the flare. (d) The diffraction of 3 mm slit.

confinement to surface plasmon and results in smaller spatial extension and propagation length. In the study conducted in ref. 25, the observed field fall-off is 28 times faster than the theoretical prediction. Because we are using the same type of Al sheet in this study, in fig. 3-14 (b), 28 is used as an empirical factor to re-plot the theoretical fall-off curve. It clearly shows a better agreement with the experiment. However, whether the factor is a frequency dependent number still remains for further investigation. When the blocking plate is in the system, the secondary diffraction in fig 3-14 (d) shows a much under-sized field pattern compared to that required by surface wave. Therefore, the coupling doesn't really happen efficiently which results in rather noisy field pattern.

In fig. 3-15 (a), the "loosely bound" field on bare metal surface has become to "tightly bound" field due to the thin layer of dielectric film. As discussed in the introduction, the thin film provides strong confinement to the surface wave energy and therefore, its spatial extension above the surface is largely reduced in all frequencies.

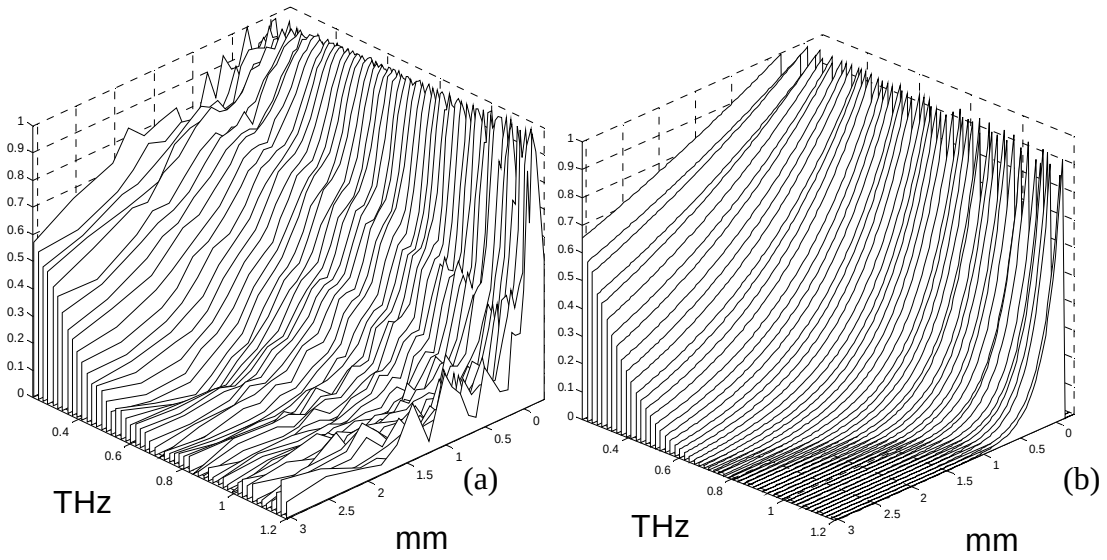

Figure 3-15. (a) Experimental surface wave fall-off on coated surface. (b) Theoretical fall off on coated surface

Excellent agreement between experiment and exponential field fall-off of dielectric-coated surface can also be observed in fig. 3-15 (a) and (b). As shown in fig. 3-16, the theoretical exponential field fall-off $e^{-\alpha y}$ and experiment field fall-off curves at a few selected frequencies are re-plotted. Again, the frequency dependent field fall-off agrees reasonably well with the corresponding theoretical fall-off.

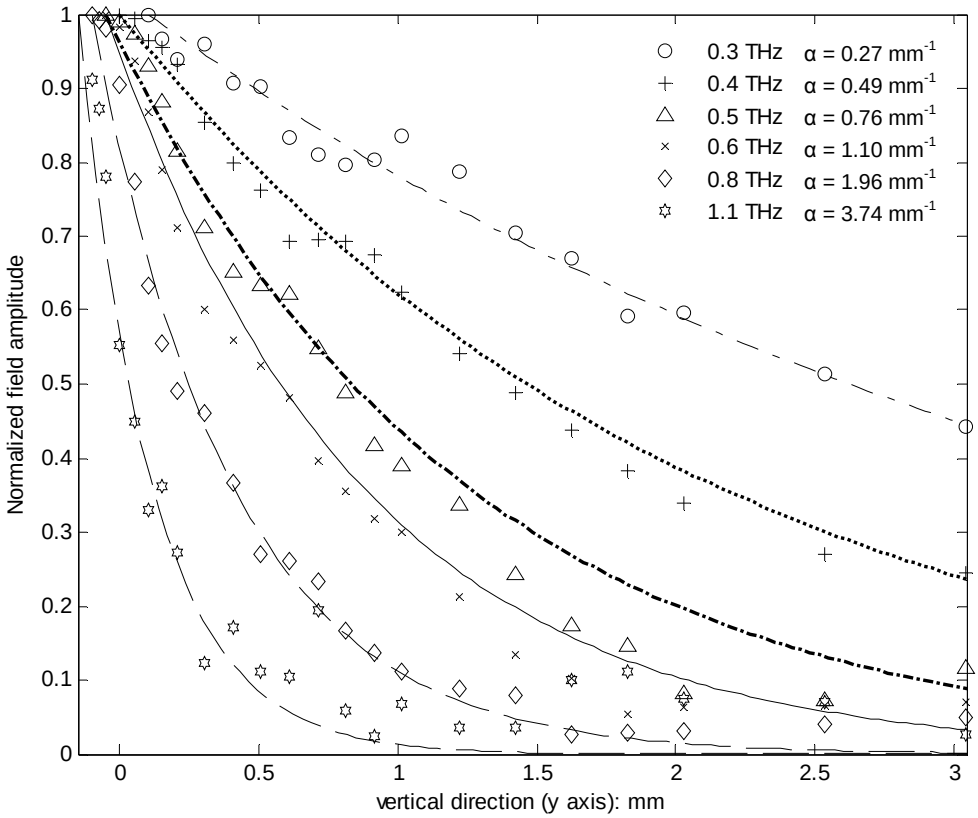

Figure 3-16. Comparison of theoretical and experimental amplitude fall-off at selected frequencies

In summary, with the dielectric film, surface plasmons exhibit a much better guided characteristic and more robust to the perturbation such as bending of the surface. The thin dielectric coating is proved to be an excellent solution to the enhancement of THz surface plasmons which is very important to the further applications of surface plasmons.

Chapter 4 Theoretical Treatment

The objective of the theoretical work is to understand the propagation process of the THz pulse on both bare metal surface and dielectric coated surface. For the bare metal surface, since the diffraction effect has been discussed in chapter 3, only the calculation of the transverse profile of the surface wave field is introduced here. For the dielectric coated surface, it includes four parts: 1. The transverse field profile of the propagating mode. With the comparison with the experimental results, this process justifies the correctness of the simplified theoretical model. 2. The dispersion relation, which accounts for the frequency dependent phase delay. This process introduces chirping into the input pulse and explains the long lasting ringing feature in the output signal. 3. The absorption. This process introduces amplitude attenuation to the input signal. 4. The coupling between different elements of the system. The last 3 processes are responsible for the reshaping of the output signal.

4.1 The surface wave field on bare metal surface

The surface wave function on metal surface contains a propagation term in the direction z along the surface and an exponential decay term in the direction of the surface normal y. Therefore, it is described as:

$$E = E_0 e^{-ik_z z} e^{-k_{ym} y} \qquad m = 1, 2 \qquad (4 - 1)$$

Where z axis is the propagation direction along the surface, y axis is the direction of surface normal. k_z is the wavevector in z direction, which is also known as propagation constant, k_{ym} is the coefficient of the exponential field fall-off in the medium on either side of the surface, here m = 1 stands for the metal and m = 2 stands for the dielectric or air. k_z and k_y can be determined using the metal-dielectric boundary conditions[41]

From the ref 41, given the complex dielectric constants on both side of the interface, the wave vectors of the surface wave have the relationships below:

$$k_z = \frac{\omega}{c}\sqrt{\frac{\varepsilon_1 \varepsilon_2}{\varepsilon_1 + \varepsilon_2}} \qquad (4 - 2)$$

$$k_z^2 + k_{ym}^2 = \varepsilon_n (\frac{\omega}{c})^2 \quad m = 1, 2 .$$

Where $\varepsilon_1 = \varepsilon_1' + i\ \varepsilon_1''$ is the complex dielectric constant of the metal, and ε_2 is the dielectric constant of the dielectric outside the metal surface, which is air in this case. ω is the angular frequency and c is the speed of light. From (4 -2) it can be seen that both k_z and k_{ym} are frequency dependent. Once k_{ym} is calculated, the theoretical field fall-off curve as fig. 3-13 (a) can be plotted.

Furthermore, the 1/e field fall-off distances (skin depth) on both sides of the interface are:

$$\delta = \frac{1}{|k_{zm}|} \qquad \mathrm{m} = 1, 2$$

$$\text{so,} \quad \delta_{air} = \frac{c}{\omega}\sqrt{\frac{\varepsilon_1 + \varepsilon_2}{\varepsilon_2^2}} \qquad (4 - 3)$$

$$\delta_{metal} = \frac{c}{\omega}\sqrt{\frac{\varepsilon_1 + \varepsilon_2}{\varepsilon_1^2}}$$

In microwave and THz range, $|\varepsilon_1''| >> |\varepsilon_1'| >> \varepsilon_2$, furthermore, the Drude complex dielectric constant of metal can be expressed to an excellent approximation as

$$\varepsilon_1 = \varepsilon_1' + i\varepsilon_1'' \approx -\frac{\sigma_{dc}}{\varepsilon_0 \Gamma} + i\frac{\sigma_{dc}}{\varepsilon_0 \omega} \qquad (4 - 4)$$

Where σ_{dc} is the dc conductivity of the metal, ε_0 is the vacuum permittivity and Γ is the damping rate. By using all the above approximations, a much simplified expression for the above skin depths can be obtained as:

$$\delta_{air} \approx \frac{c}{\omega}\frac{\sqrt{2\varepsilon_1''}}{\varepsilon_2} = \sqrt{\frac{2\sigma_{dc}}{\omega^3 \varepsilon_0^2 \mu_0}} \qquad (4 - 5)$$

$$\delta_{metal} \approx \frac{c}{\omega}\sqrt{\frac{2}{\varepsilon_1''}} = \sqrt{\frac{2}{\omega \mu_0 \sigma_{dc}}}$$

4.2 The surface wave field on dielectric coated surface

4.2-1 The transverse field profile

The dielectric coated metal surface structure is shown in the fig. 4-1 (a). General modal analysis to this 3-layer structure is often complicated in theory because of the complex

metal conductivity [15, 17, 22]. However, in THz range the problem can be viewed in a much simpler way.

In THz range, the real part of the metal conductivity is high and can be considered to be frequency independent constant and to be equal to the handbook dc value (for aluminum, $\sigma_r = 4 \times 10^7$ S/m), in contrast to metallic conductivity at optical frequencies, at $\lambda = 800$ nm, $\sigma_r = 1.2 \times 10^5$ S/m [42]. Therefore, as shown in the fig. 4-1 (a), the dielectric coated metal surface can be viewed as a classic waveguide structure --- dielectric slab waveguide on perfect conductor, also called grounded dielectric film waveguide. To solve the wave field in this type of waveguide, the perfect conductor plane can be treated as a symmetric plane. Then the problem is equivalent to solving a waveguide that is combined by the film and its mirror image, which is actually a free-standing dielectric slab waveguide with twice thickness as shown in fig. 4-1 (b). Therefore, the problem

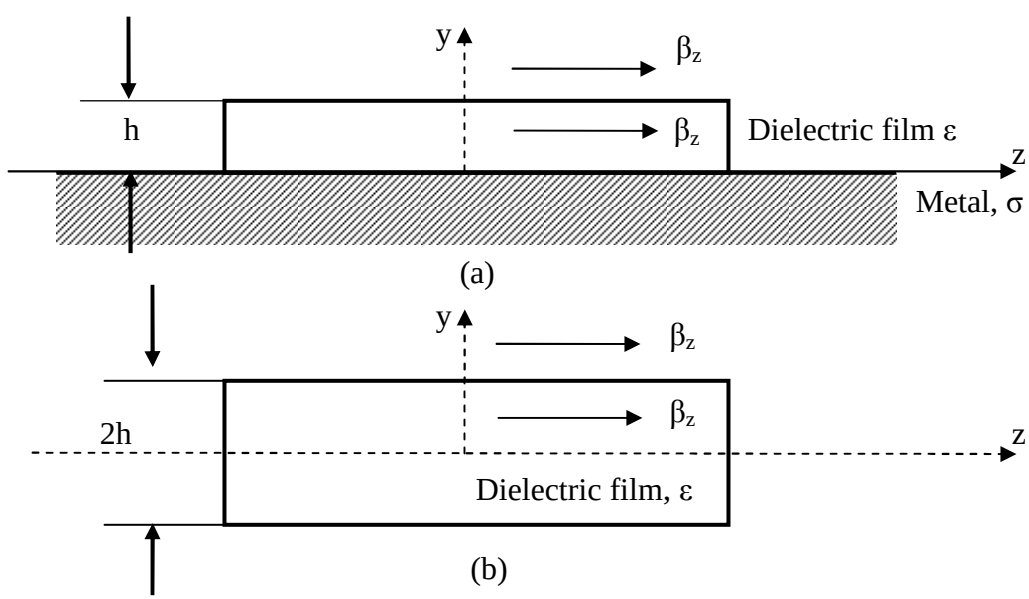

Figure 4-1. Theoretical model equivalence of slab waveguide structure, if the conductivity in (a) is infinite, then its field distribution is equivalent to the upper half of (b)

of the surface wave is simplified to the model analysis of a dielectric slab waveguide. The detailed solution of modes and wave vectors is standard and can be found in appendix I.

Both theoretical [2] and experimental work [43] has shown that in our very thin (~*λ/20*) dielectric slab waveguide setup, only the dominant TM_0 mode is coupled into the waveguide and therefore our surface waveguide structure is working in single mode propagation. According to the field solution in Appendix I, the transverse electrical field inside the slab has cosine form while the field outside the slab decays exponentially (evanescent wave). Therefore, once the transverse field fall-off constant and the wave vector are calculated, the problem is then solved.

The left chart in fig. 4-2 shows a typical TM_0 mode E_y field solution of a 25 μm dielectric slab (n = 1.5) waveguide at 0.5 THz. Inside the film, the E_y field is a small portion of a cosine curve which falls off from its apex. At the dielectric-air boundary, the

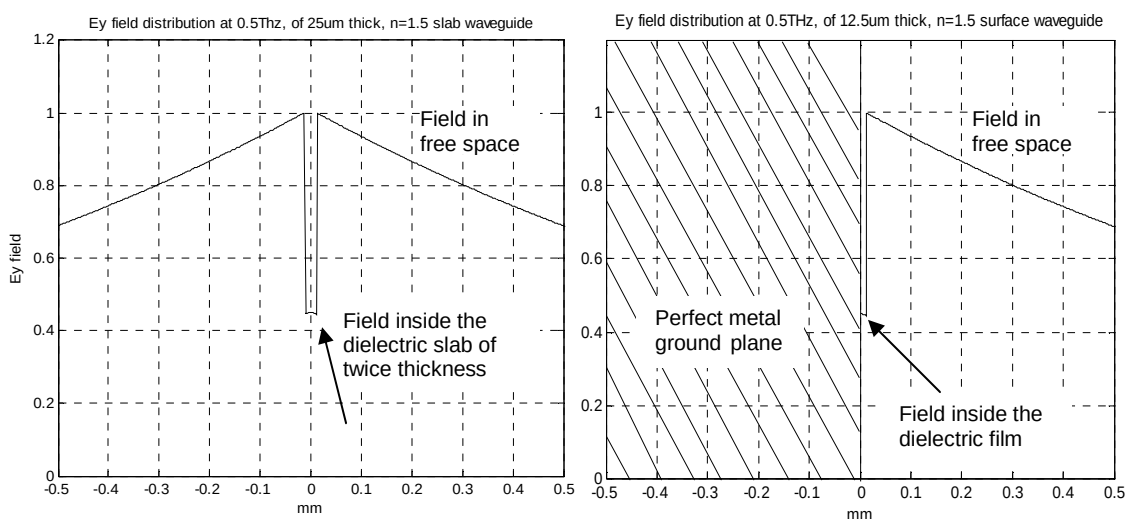

Figure 4-2. left: E_y field TM_0 distribution at 0.5 THz of a plastic slab waveguide; right: field profile of coated surface. (n =1.5)

E_y field has a jump because of the discontinuity of the dielectric constant. Outside the film, the E_y field fall-off is the function $e^{-\alpha_{yo}y}$ where the fall-off constant α_{yo}= 7.64 cm^{-1}. As for our case, which is a metal surface overcoated structure with 12.5 μm dielectric film, the field profile on the right is half of that of dielectric slab waveguide on the left.

In the dielectric slab structure, electromagnetic fields propagate in the TM_0 mode both inside and outside the slab with the same wave vector. Therefore, although a perfect conductor does not support the surface wave, when it is covered with a thin dielectric film, a guided surface wave can be established. Thus, the wave that is propagating on the dielectric coated metal surface is in fact the same as the guided mode of the corresponding dielectric waveguide. The surface wave here is the same as the evanescent field of the guided mode outside the dielectric layer.

As shown in fig. 4-3, the exponential fall-off outside the film is plotted against frequency to compare with the experimental measurement shown in fig. 3-15 (b). Because our sample film is only 12.5 μm thick, the cosine function inside the film is not detectable.

Our approach of treating metal as a perfect conductor at THz frequencies has greatly simplified the problem. Earlier researchers solved the general wave equation of the

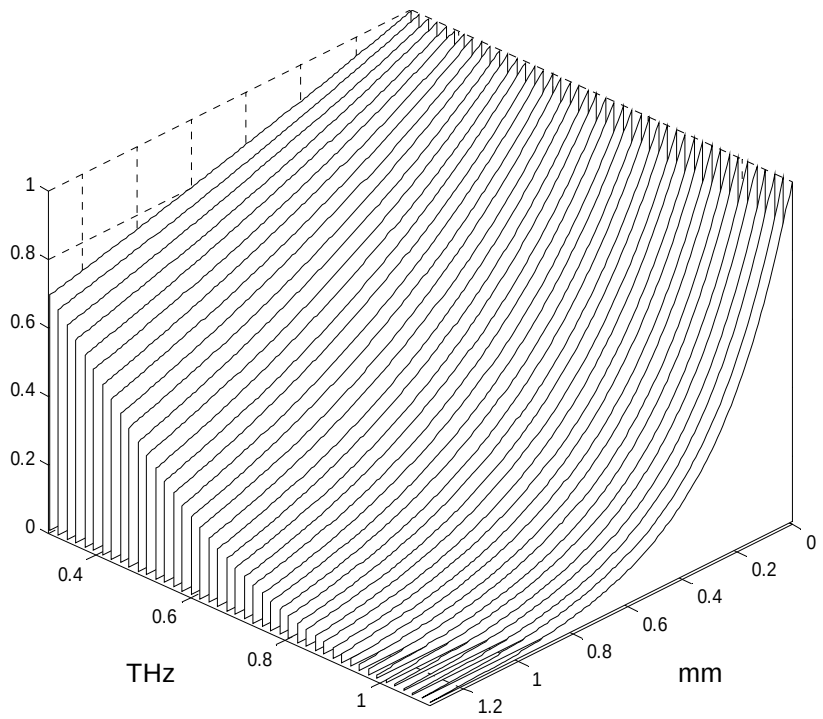

Figure 4-3. Theoretical normalized surface wave fall-off curve

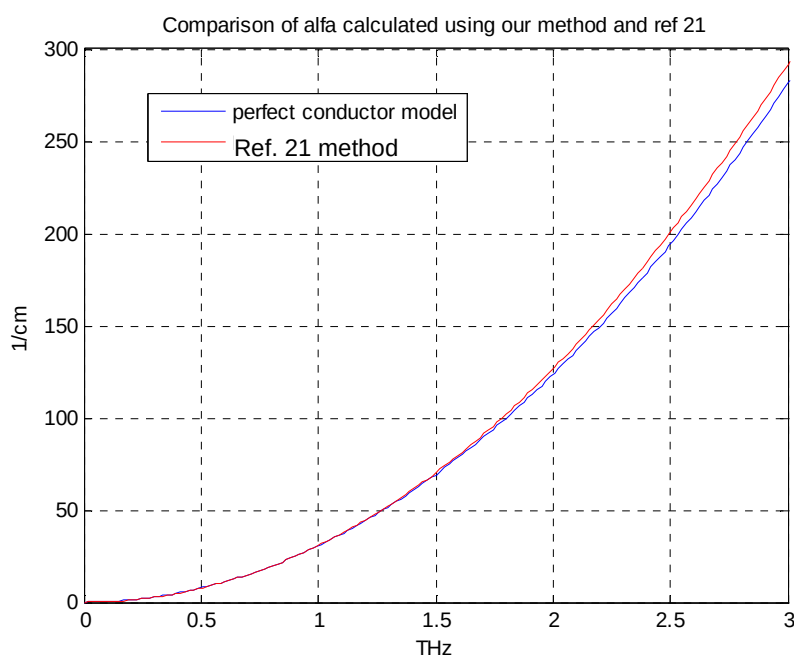

Figure 4-4. Exponential field fall-off constants calculated with and without perfect conductor assumption

surface wave on coated metal using the actual frequency dependent metal dielectric constant, which must be used for the optical range[22]. The general solutions of exponential fall-off decay constants on coated metal are compared to our simplified solutions in fig. 4-4. Not surprisingly the two curves almost overlap which proves that the perfect-conductor treatment is an accurate assumption in THz, similar to the usual approach in microwave theory to derive the modes of metal waveguides.

4.2-2 The dispersion

Using the method described in Appendix I, the frequency dependent wave vector $\beta_z(\omega)$ of the guided mode can be calculated. Therefore, given the propagation length, the frequency dependent phase delay can be calculated.

If the signal at the input end of the film waveguide is described using its electrical field: $E_{ref}(\omega)$, then at the output end, the electrical field $E_{out}(\omega, z)$ can be written as [43]:

$$E_{out}(\omega, z) = E_{ref}(\omega) TC \; e^{-i\beta_z z} e^{-\alpha z} \qquad (4 - 6)$$

Where ω is the angular frequency, β_z is the wave vector of the surface wave mode at ω. Both the wave inside the film and outside the film propagates with the same wave vector. α is the amplitude attenuation of the waveguide at ω. T is the transmission coefficient, C is the coupling coefficient.

As discussed previously, the dispersion in signal pulse can be understood in the dispersion of the dielectric slab waveguide whose field distribution is frequency dependent. Therefore, the fraction of power that propagates inside and outside the dielectric slab is also a function of frequency. The fraction of power can be calculated using the mode parameter method in Appendix 1. The higher the frequency, the bigger fraction of power is held inside the slab. Furthermore, bigger portion of energy inside the slab, the closer the propagation speed to the speed of light of bulk dielectric; the less portion of energy inside the slab, the closer the propagation speed to the speed of light in free space. This explains why in the surface wave signal on dielectric coated surface, the lower frequency components travel faster than the higher frequency ones.

Once $\beta_z(\omega)$ is obtained, the phase velocity $v_p = \omega / \beta_z$, and the group velocity $v_g = d\omega / d\beta_z$ [2]. Fig. 4-5 shows the calculated group velocity and phase velocity as functions of frequency. Both group velocity and phase velocity decrease as frequency increases, which is in agreement with the experimental results.

With respect to the energy exchange between the TSW and the freely propagating diffracted wave traveling at c, the coherence length L_c at 0.5 THz from fig. 4-5 is $\lambda/2 = 0.0025\ L_c$, $L_c = 200\lambda$, $L_c = 120$ mm or 12 cm which is ½ our guided wave path, consequently the waves can decouple. At 1 THz the coherence length shortens considerably to $\lambda/2 = 0.01\ L_c$, $L_c = 50\lambda = 50 \times 0.3 = 15$ mm = 1.5 cm.

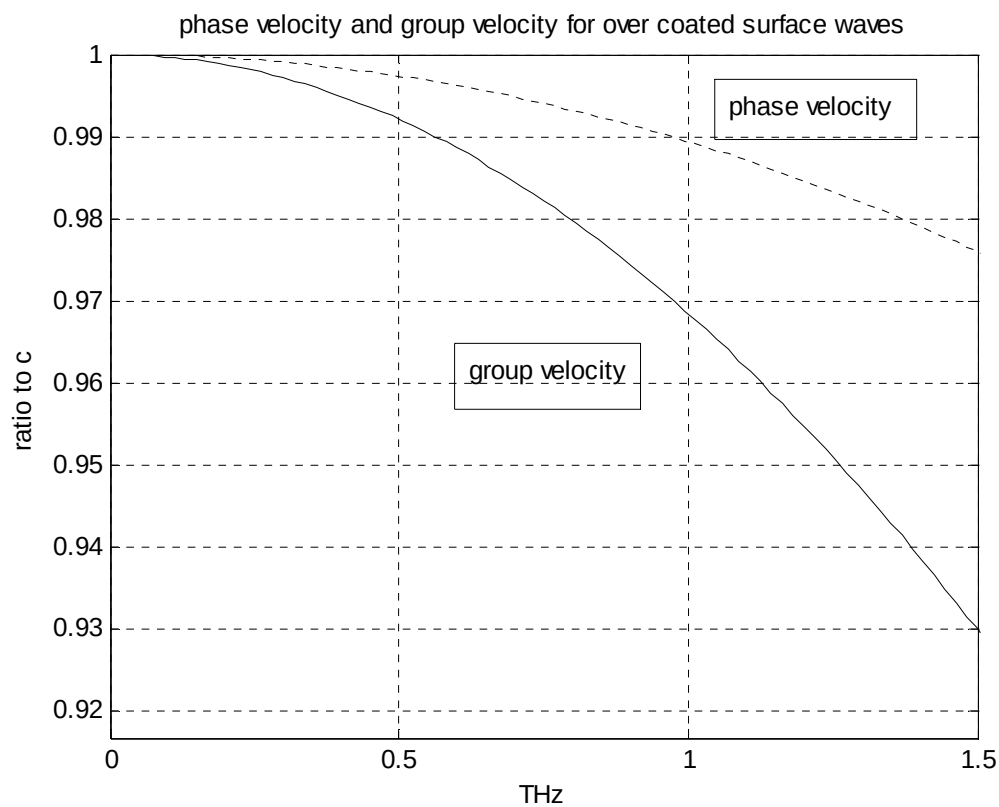

Figure 4-5. Group velocity and phase velocity ratio to speed of light of the fundamental TM_0 mode of dielectric slab waveguide with a thickness of 25 μm and an index of refraction of 1.5

Therefore, when the $\beta_z(\omega)$ is obtained, the phase change due to the propagation can be calculated as $\beta_z L$ where L is the length of the thin film waveguide which is 20 cm in our case. The phase delay as a function of frequency will be applied to the phase term of the corresponding frequency of the input signal spectrum. The amplitude term will be discussed in the next two sections.

4.2-3 The absorption coefficients

The absorption α of the thin film over-coating contains two parts: the absorption of the dielectric film $\alpha_{g,L}$ and the absorption of the metal due to its finite conductivity α_m.

$$\alpha = \alpha_{g,L} + \alpha_m \qquad (4 - 7)$$

1) The dielectric absorption $\alpha_{g,L}$

Based on the definitions of model parameters in equation (5) to (8) in appendix I, we have V, U, W and Δ as model parameters. Then using these parameters, in ref [1], the fraction of power in the core can be calculated:

$$\eta = 1 - \frac{n_{co}^2 n_{cl}^2 U^2}{n_{co}^2 n_{cl}^2 V^2 + n_{co}^4 W^3 + n_{cl}^4 W U^2} \qquad (4 - 8)$$

Fig. 4-6 shows the fraction of power as a function of frequency for our 12.5μm surface waveguide structure.

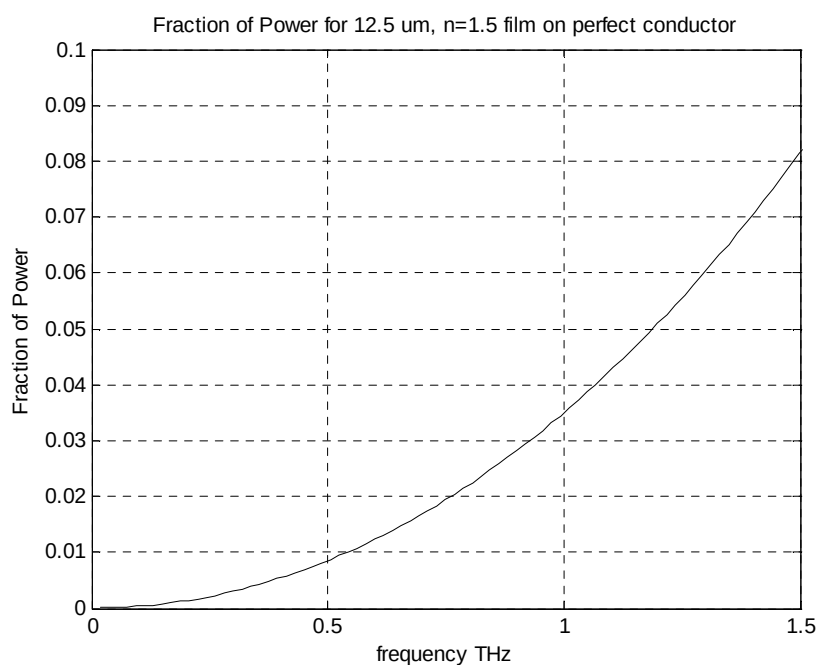

Figure 4-6. Fraction of power (η) at different frequencies in our surface structure

The power absorption coefficient due to the dielectric layer is [44]:

$$\alpha_{g,l} = \eta \alpha_l \frac{v_l}{v_g} \qquad (4 - 9)$$

Where α_l is the absorption of the bulk dielectric, in our experiment, the dielectric is polyethylene, whose absorption is lower than 1 cm^{-1} [45]. In this calculation we use frequency independent value 1 cm^{-1} as the value of α_l. v_l is the group velocity of bulk material and v_g is the mode group velocity within the waveguide layer. We have [1]:

$$v_l = c / n_{co}$$

(pg 243, table 12-2[1]) (4 - 10)

$$v_g = \frac{c}{n_{co}^2} \frac{\beta}{k} \frac{1}{1 - 2\Delta(1-\eta)}$$

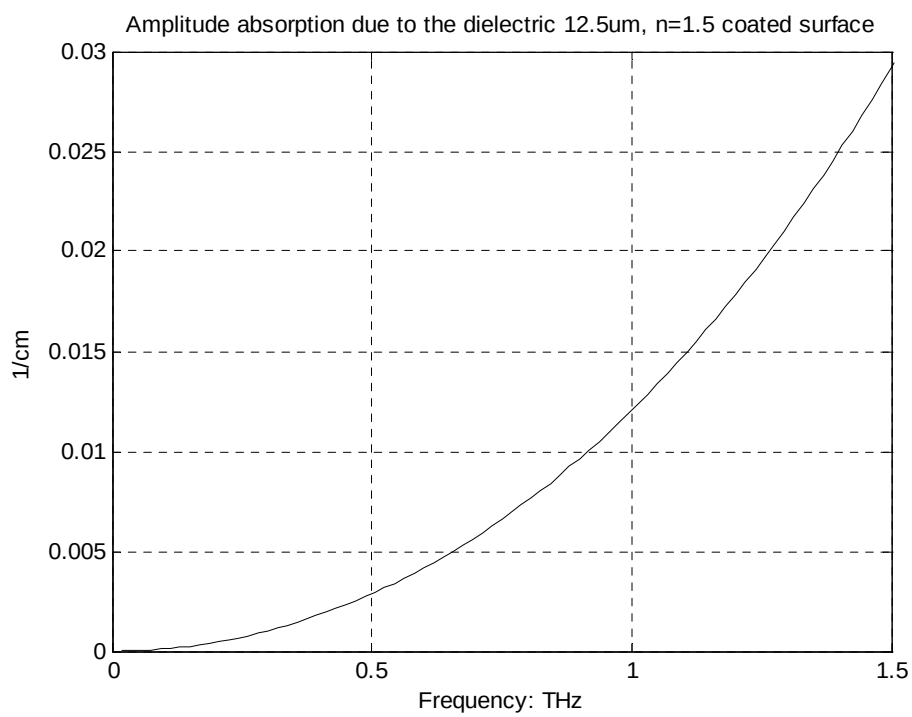

Figure 4-7. Amplitude absorption due to the dielectric layer

Given fraction of power (η) and group velocities, using equation 5, the amplitude absorption $\alpha_{g,l}/2$ due to the dielectric layer can be calculated as a function of frequency, as shown in fig. 4-7.

2) The metal absorption α_m

i) Analytical method

The Joule heat is generated by the surface current induced by the surface wave mode field near the metal. This can be treated using a simple approximation method. The detail analytic calculation is described in the Appendix III. The analytic result for the metal absorption can be written as:

$$\alpha_m/2 = \sqrt{\frac{\omega\mu_0}{2\sigma}}\frac{\omega n^2\varepsilon_0}{4h\omega\sqrt{\mu_0\varepsilon_0}}\eta = \sqrt{\frac{\pi c}{\lambda\sigma}}\frac{n^2\sqrt{\varepsilon_0}}{4h}\eta \qquad (4 - 11)$$

In below figure, the amplitude absorption due to the metal is plotted.

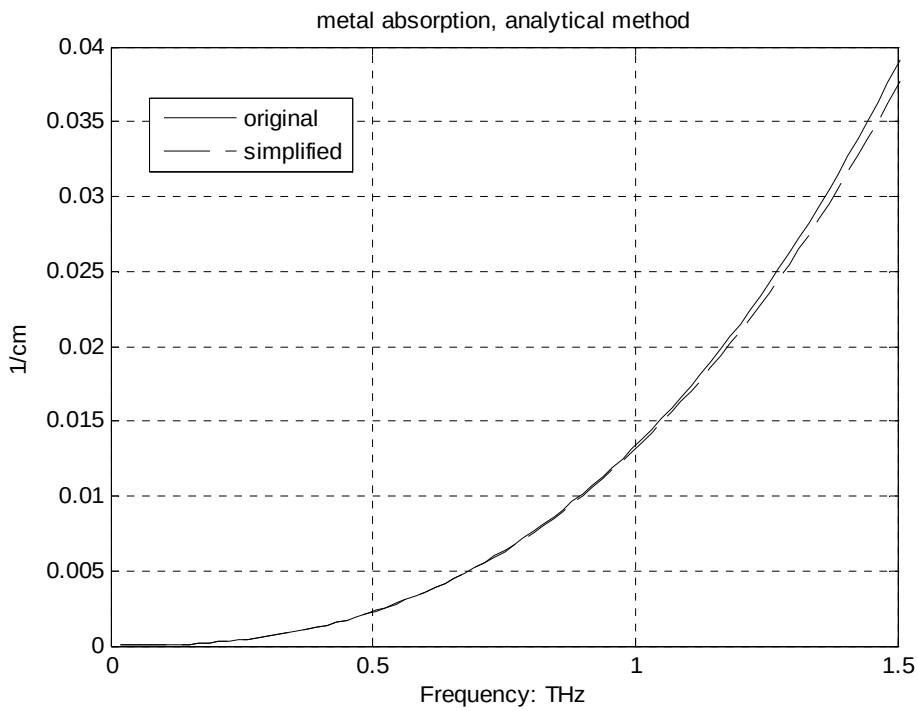

Figure 4-8. Amplitude absorption due to metal $\alpha_m/2$ using analytical method

ii) Approximation method:

To simplify the calculation, the metal absorption can also be approximated using the metal absorption of dielectric filled parallel plate waveguide (PPWG). Consider the dielectric coated surface wave guide system as a PPWG with top plate removed. Details are introduced in appendix III. The obtained approximation is:

$$\alpha_m^{SW} = 0.5\eta\alpha_m^{PPWG}\frac{v_l}{v_g} \approx 0.5\eta\alpha_m^{PPWG}\Big/ n \qquad (4 - 12)$$

This result gives the amplitude attenuation constant (due to the metal) of the surface wave as fig. 4-9 shows the curve of α_m^{SW} versus frequency which agrees well with the result of the analytical method in fig. 4-8:

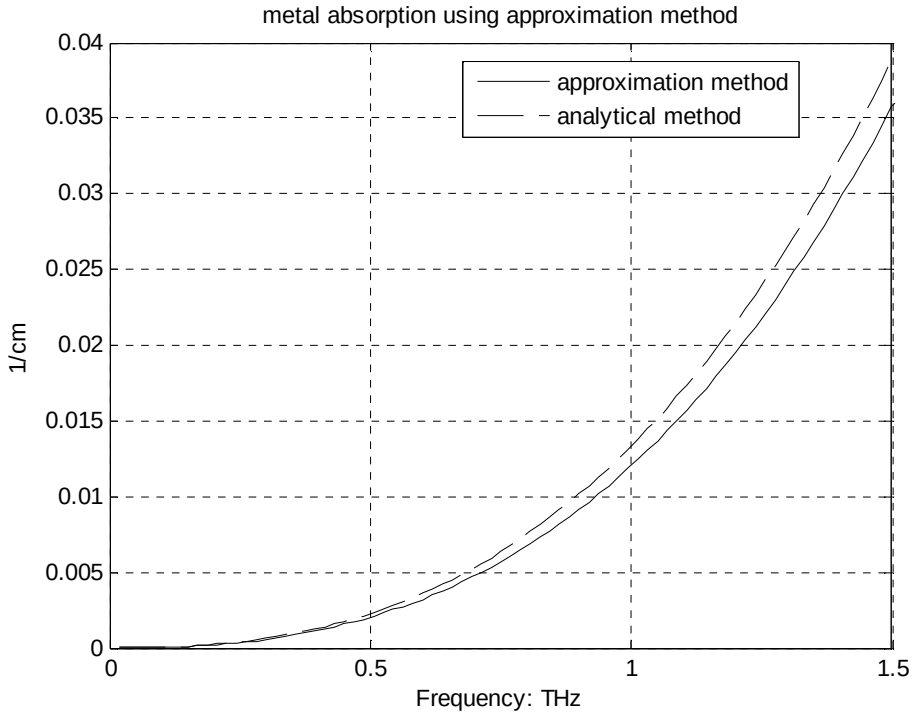

Figure 4-9. Metal amplitude absorption calculated using approximation method

4.2-4 The coupling coefficient

When THz pulse propagates in the surface wave apparatus, it will go through a number of junctions of different waveguide elements, such as cylindrical lens coupling to parallel plate waveguide (PPWG) and PPWG to thin film coated surface waveguide. At each junction, THz energy is transferred from one element to the other. Since the energy is carried by guided modes of the corresponding elements, the coupling at the junctions is eventually the coupling of modes between different waveguide elements.

Two coupling processes are considered here: 1. The coupling between the PPWG and the thin film surface waveguide. 2. The coupling at the aluminum sheet block.

The well-known overlap integral is used to calculate the power coupling coefficient between two waveguide elements [46].

$$A = \frac{[\int \vec{E}_1 \cdot \vec{E}_2^{\,*} ds]^2}{\int |E_1|^2 ds \int |E_2|^2 ds} \qquad (4 - 13)$$

Where E_1 and E_2 are the mode fields of the two waveguides, s denotes the integration over the waveguide cross section. Here A is the normalized power coupling coefficient; the amplitude coupling coefficient is the square root of A.

1). The coupling between the PPWG and the thin film surface waveguide.

As fig. 4-10 shows, this process contains two steps: (1) Quasi-TEM mode in the PPWG couples into the quasi-TEM mode in the flare, which can be considered as an adiabatic structure PPWG. (2) the quasi-TEM mode in the flare couples into the surface TM_0 mode of the surface waveguide. For region (1), according to the work of J. Zhang and Grischkowsky, the coupling can be considered to be unity for adiabatic compression shape waveguide [35]. So its coupling coefficient is not calculated. For region (2), the E_y field of the quasi-TEM in the flare and the TM_0 mode in the thin film surface waveguide are shown in (4 - 14) and fig. 4-11:

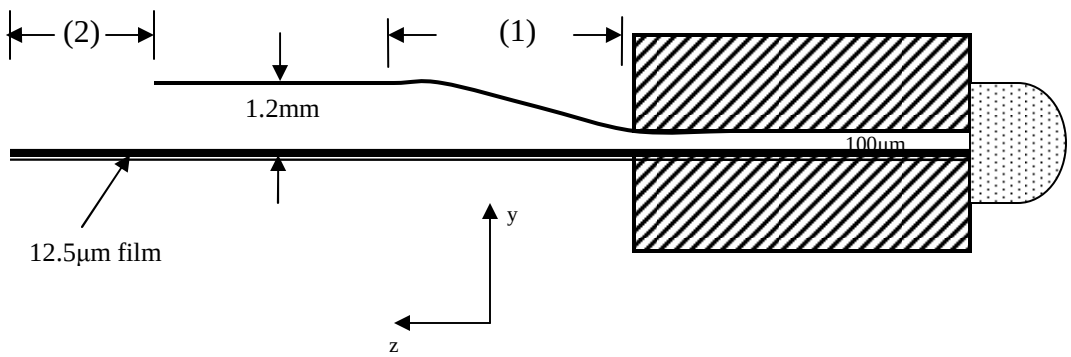

Figure 4-10. Zoomed drawing of the PPWG-Surface wave junction

$$E_{y1} = \begin{cases} 1 & 0 < y < 12.5\ \mu m \\ 2.25 & 12.5\ \mu m < y < 1.2\ mm \\ 0 & y > 1.2\ mm \end{cases} \qquad E_{y2} = \begin{cases} \cos(\beta_{yd} y) & 0 < y < 12.5\ \mu m \\ e^{-\alpha_{y0} y} & 12.5\ \mu m < y < \infty \end{cases} \qquad (4 - 14)$$

The detailed definitions of the parameters are listed in the appendix.

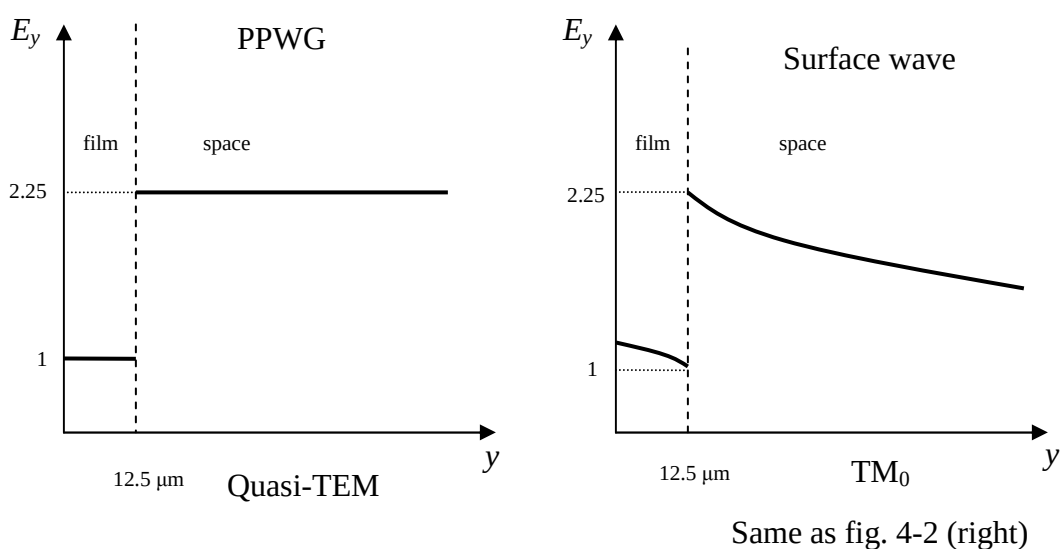

Figure 4-11. Electric field functions of the two coupling modes

In PPWG, the E field is perpendicular to the waveguide plates and has the same value over the entire cross section. When the bottom plate is covered by a thin film, the E field in the space can still be considered to be the same as the film can be treated as perturbation. However, the field in the film needs to satisfy the boundary condition, namely, the ratio of the E field inside and outside the film should equal to the inverse ratio of the dielectric constants. In our case the ratio is 2.25. The calculated normalized amplitude coupling coefficient is shown in fig. 4-12.

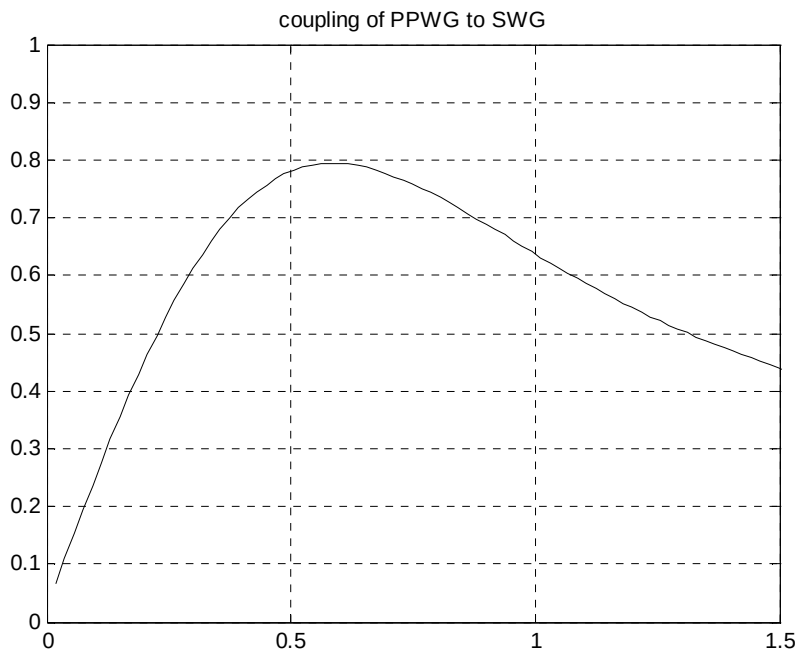

Figure 4-12. The calculated amplitude coupling coefficient of PPWG – SWG junction

2). The coupling at the aluminum sheet block

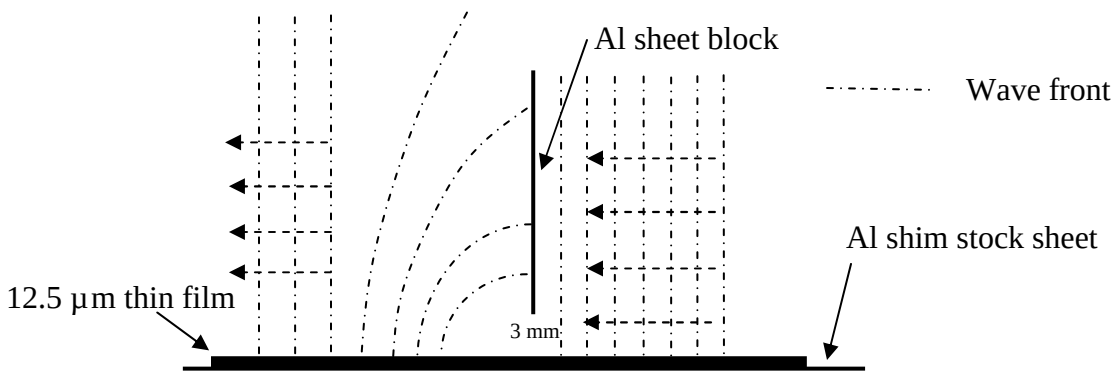

Figure 4-13. Schematic of the wave propagation at the slit

When the surface wave is propagating along the dielectric coated surface, as discussed previously, its field extension into the free space above the surface is frequency dependant. Lower frequency component has longer extension. When the wave runs into the aluminum sheet block as shown in fig. 2-2 and fig. 4-13, the wave front will be

$$E_{y1} = \begin{cases} \cos(\beta_{yd} y) & 0 < y < 12.5\ \mu m \\ e^{-\alpha_{y0} y} & 12.5\ \mu m < y < \infty \end{cases}$$

(4 - 15)

$$E_{y2} = \begin{cases} \cos(\beta_{yd} y) & 0 < y < 12.5\ \mu m \\ e^{-\alpha_{y0} y} & 12.5\ \mu m < y < 3mm \\ 0 & y > 3\ mm \end{cases}$$

truncated by the block. Only the part of the wave that is below the slit height (3 mm in our experiment) can pass through and re-establish the surface wave. In other words, the

aluminum block acts as a spatial window filter which can be described using a binary function and applied to the overlap integral to calculate the coupling coefficient. The two E fields for overlap integral are shown mathematically in (4-15) and graphically below:

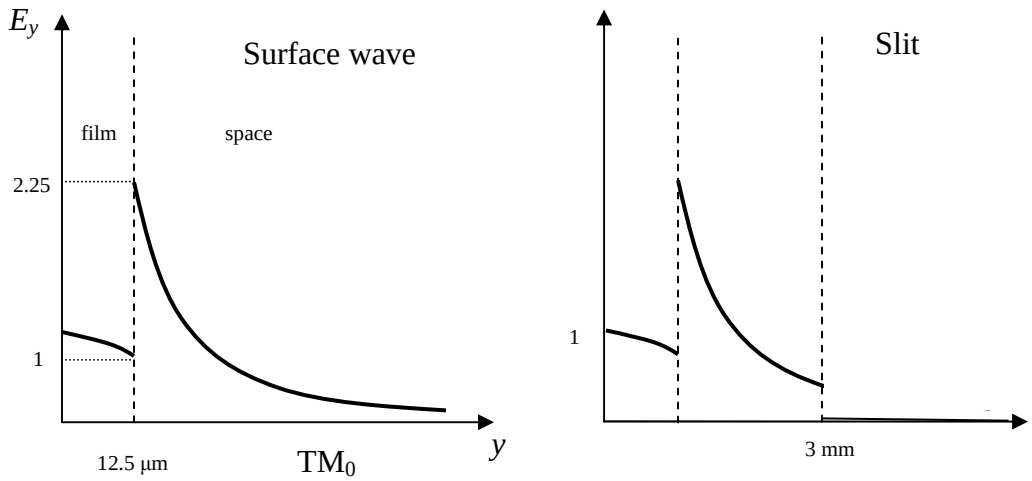

Same as fig. 4-2 Mode field of the slit

Figure 4-14. Electric field functions of the two coupling modes at the slit

The calculated amplitude coupling coefficient of the slit is shown in the fig. 4-15. Because the thickness of the slit is negligible, it works as a perfect block which maintains the part of the wave front that falls onto the slit and completely blocks the rest part that falls onto the metal sheet. Therefore, the function for the slit is the same as the input wave front in the slit opening area and is zero at rest part. As shown in the right fig. 4-15. The product of the above two coupling coefficients gives the parameter C in the equation (4 - 6).

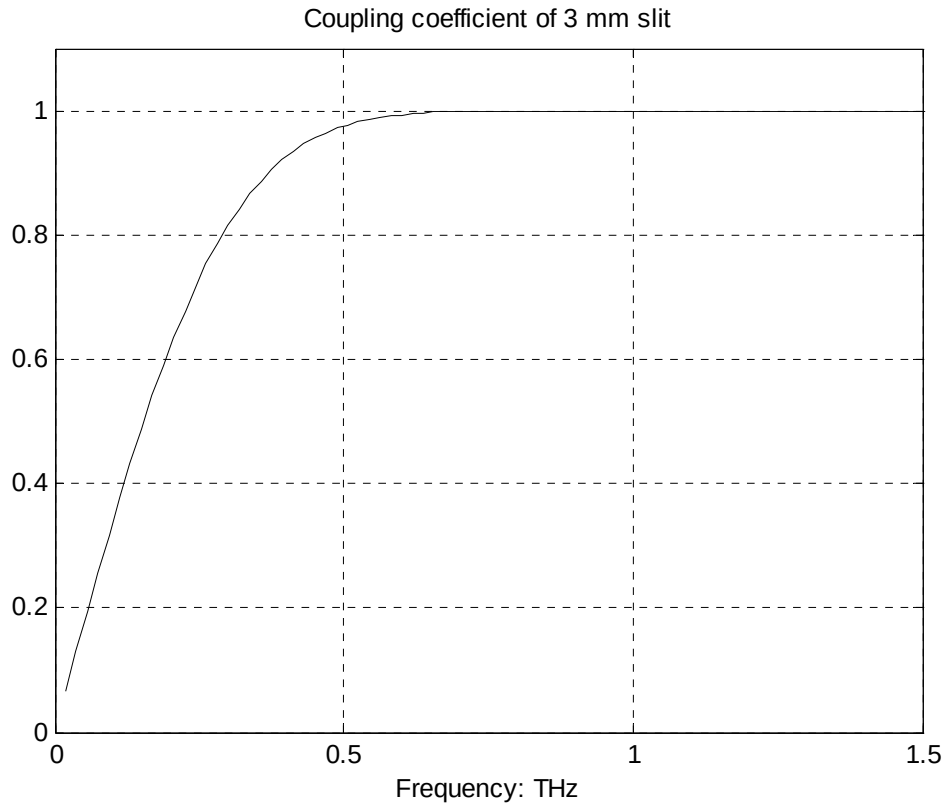

Figure 4-15. The calculated amplitude coupling coefficient of the slit

So far the main mechanisms that are responsible for the signal reshaping have been calculated. It includes the absorption of the dielectric material and metal, the dispersion in the film and the coupling coefficient at the main junctions. The Fresnel's transmission coefficient of the silicon cylindrical lens is also estimated to be 70%. Other uncalculated coefficients are believed to be frequency independent factors and will only have slight effect on the pulse magnitude. Therefore, given a free space reference signal, the output signal can be theoretically worked out. In fig. 4-16, it shows comparison of theoretical output surface wave spectrum and the actual experimental surface wave spectrum. The two spectra are normalized to match their peaks for comparison.

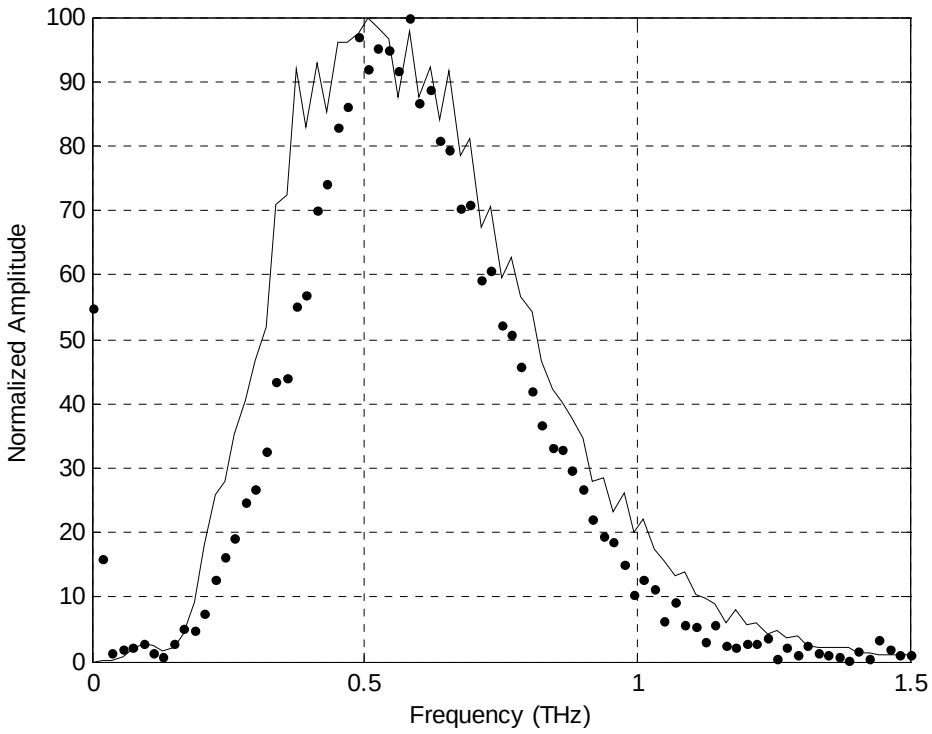

Figure 4-16. The theoretical output spectrum (solid line) and experimental output spectrum (dot) on dielectric coated surface

The calculated spectrum shows good agreement with the experimental spectrum. From the figure, compare with the experimental spectrum (dotted curve), the theoretical one (solid curve) has more low frequency component remaining than the experimental one. We believe this is because that waveguiding system always works as a high-pass filter, in which lower frequency is much easier to get disturbed since it has more energy propagates as the fringing field and there are still a few loss factors not yet considered due to the system complexity.

Finally, inverse Fourier transform is performed to the calculated spectrum so that the theoretical time domain signal can be obtained. In the above figure, the solid theoretical time domain curve is compared to the red dotted time domain experimental signal.

Excellent agreement is obtained which shows that the surface wave on dielectric coated surface is well understood.

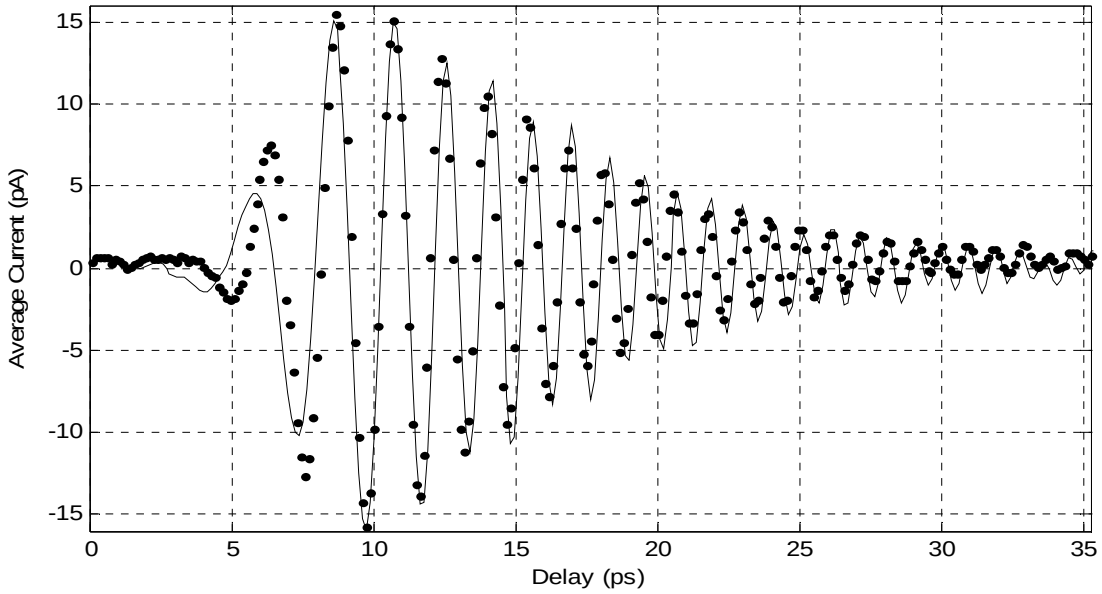

Figure 4-17. The comparison of time domain curves between experimental (dot) and theoretical (solid line)

Chapter 5 Conclusions

The objective of this project is to study the propagation of THz surface waves and the field confinement effect of the dielectric coating. During the past one and half years, standard THz-TDS system was modified to be capable of measuring the transverse electrical field in subwavelength resolution. A good quality thin film coated aluminum sample was made and THz surface wave field profile was measured for the first time. The experimental results are analyzed in both time domain and frequency domain. Theoretical models were built and have excellent agreement with the experimental results. Compared with general surface wave model, our approach provides a much simpler way of calculation with better physical insight and no loss of accuracy.

In the experimental part, the uniqueness of the THz wave granted the success of this study. In microwave and lower radio frequency range, the long wavelength and high metal conductivity make it more difficult to bind the surface wave. In the optical range, on the other hand, the short wavelength and low metal conductivity make the surface wave field difficult to observe. The THz wavelength enables reasonable dimensions of sample size and measurement range. Metal still has high conductivity in THz frequency so that significant changes in surface wave confinement can be observed.

In our study, the THz surface system is modified to make the receiver movable so that the surface wave field distribution can successfully measured in subwavelength scale. The sample of metal sheet with a tightly attached subwavelength dielectric layer was successfully made. Comparing with the bare metal surface measurement, the surface wave on the dielectric coated surface is significantly compressed to a few wavelength ranges. The THz surface wave field pattern was directly measured for the first time.

In the theoretical part, we developed an improved simple approach for THz surface waves on both bare metal surface and dielectric coated surface. In the past, the wave equations of surface wave on dielectric coated metal surface have complicated forms because the complex metal dielectric constant introduces more complicated boundary conditions. With the perfect conductor assumption in THz range, the metal boundary can be conceptually removed and the film coating on metal surface becomes equivalent to dielectric slab waveguide with twice thickness. The solutions to the latter have relatively simple forms which maintain the high accuracy. The theoretical model based on the perfect conductor assumption is proved to be correct and much simpler than the general equation solving method. Therefore in THz, the complicated dielectric coated metal surface can be studied using the classical mode analysis for dielectric slab waveguide.

Chapter 6 Future Work

The study has demonstrated the effect of a thin dielectric layer on the THz surface wave. The success of this study has opened THz surface wave research in two ways:

First, dielectric coating has shown extraordinary effectiveness in enhancing the surface wave attachment to the metal surface. Precise characterization of the film coating has provided the possibility of a new technique in high sensitivity THz surface wave spectroscopy.

Second, recent surface wave or surface plasmon studies mostly focus on the transmission or reflection property in the surface normal direction in the far field. The experimental study presented here demonstrates a new approach of high precision near field study in the direction along the surfaces which could offer more fundamental understanding and physical insight to the surface wave phenomena. For example, the intensively studied transmission enhancing hole arrays can be studied in this system to measure the surface wave propagation between the hole arrays. Together with the theory of overlap integral of surface waves [29], it can explain the mechanism of the enhanced transmission.

Reference

1. Snyder, A.W. and J.D. Love, *Optical Waveguide Theory*. 2000: Kluwer Academic Publishers.
2. Balanis, C.A., *Advanced Engineering Electromagnetics*. 1989: Wiley.
3. Sommerfeld, A., *Über die Fortpflanzung ebener electrodynamischer Wellen längs eines Drahtes.* Annalen der Physik und Chemie, 1899(67): p. 233.
4. Zenneck, J., *Über die Fortpflanzung ebener elektromagnetischer Wellen längs einer ebener Leiterfläche und ihre Beziehung zur drahtlosen Telegraphie.* Annalen der Physik 1907(23): p. 846.
5. Barlow, H.M. and A.L. Cullen, *Surface Waves.* The Proceedings of the Institute of Electrical Engineers, 1953. **100**: p. 329.
6. Barlow, H.M. and J. Brown, *Radio surface waves*. International monographs on radio. 1962, Oxford: Clarendon Press.
7. Otto, A., *Excitation of nonradiative surface plasma waves in silver by the method of frustrated total reflection.* Zeitschrift für Physik A Hadrons and Nuclei, 1968. **216**(4): p. 398-410.
8. Raether, H., *Surface Plasmons and Roughness*, in *Surface Polaritons*, V.M. Agranovich and D.L. Mills, Editors. 1982, NORTH-HOLLAND PUBLISHING COMPANY: AMSTERDAM - NEW YORK - OXFORD. p. 331.
9. Ebbesen, T.W., et al., *Extraordinary optical transmission through sub-wavelength hole arrays.* Nature, 1998. **391**(6668): p. 667-669.
10. Huang, C.-P. and Y.-Y. Zhu, *Plasmonics: Manipulating Light at the Subwavelength Scale.* Active and Passive Electronic Components, 2007. **2007**: p. 13.

11. Hasegawa, K., J.U. Nockel, and M. Deutsch, *Curvature-induced radiation of surface plasmon polaritons propagating around bends.* Physical Review A (Atomic, Molecular, and Optical Physics), 2007. **75**(6): p. 063816-9.
12. Yin, L., et al., *Surface plasmons at single nanoholes in Au films.* Applied Physics Letters, 2004. **85**(3): p. 467-469.
13. Klopfleisch, M. and U. Schellenberger, *Experimental determination of the attenuation coefficient of surface electromagnetic waves.* Journal of Applied Physics, 1991. **70**(2): p. 930-934.
14. Goubau, G., *Surface Waves and Their Application to Transmission Lines.* Journal of Applied Physics, 1950. **21**(11): p. 1119-1128.
15. Attwood, S.S., *Surface-Wave Propagation Over a Coated Plane Conductor.* Journal of Applied Physics, 1951. **22**(4): p. 504-509.
16. Schlesinger, Z., B.C. Webb, and A.J. Sievers, *Attenuation and coupling of far infrared surface plasmons.* Solid State Communications, 1981. **39**: p. 1035.
17. Stegeman, G.I. and R.J. Seymour, *Surface plasmon attenuation by thin film overlayers in the far infrared.* Solid State Communications, 1982. **44**(9): p. 1357-1358.
18. Ufimtsev, P.Y., R.T. Ling, and J.D. Scholler, *Transformation of surface waves in homogeneous absorbing layers.* Antennas and Propagation, IEEE Transactions on, 2000. **48**(2): p. 214-222.
19. Ling, R.T., J.D. Scholler, and P.Y. Ufimtsev, *The Propagation and Excitation of Surface Waves in an Absorbing Layer.* Journal of Electromagnetic Waves and Applications, 1998. **12**(7).
20. Ling, R.T., J.D. Scholler, and P.Y. Ufimtsev, *Errata On: the Propagation and Excitation of Surface Waves in an Absorbing Layer.* Journal of Electromagnetic Waves and Applications, 2000. **14**(10).

21. Ufimtsev, P.Y. and R.T. Ling, *New results for the properties of TE surface waves in absorbing layers.* Antennas and Propagation, IEEE Transactions on, 2001. **49**(10): p. 1445-1452.

22. Schlesinger, Z. and A.J. Sievers, *IR surface-plasmon attenuation coefficients for Ge-coated Ag and Au metals.* Physical Review B (Condensed Matter), 1982. **26**(12): p. 6444-6454.

23. Mills, D.L. and A.A. Maradudin, *Surface corrugation and surface-polariton binding in the infrared frequency range.* Physical Review B, 1989. **39**(3): p. 1569.

24. Hibbins, A.P., J.R. Sambles, and C.R. Lawrence, *Grating-coupled surface plasmons at microwave frequencies.* Journal of Applied Physics, 1999. **86**(4): p. 1791-1795.

25. Jeon, T.-I., J. Zhang, and D. Grischkowsky, *THz Sommerfeld wave propagation on a single metal wire.* Applied Physics Letters, 2005. **86**(16): p. 161904-3.

26. Jeon, T.-I. and D. Grischkowsky, *THz Zenneck surface wave (THz surface plasmon) propagation on a metal sheet.* Applied Physics Letters, 2006. **88**(6): p. 061113-3.

27. O'Hara, J., R. Averitt, and A. Taylor, *Prism coupling to terahertz surface plasmon polaritons.* Opt. Express, 2005. **13**(16): p. 6117-6126.

28. Qu, D., D. Grischkowsky, and W. Zhang, *Terahertz transmission properties of thin, subwavelength metallic holearrays.* Opt. Lett., 2004. **29**(8): p. 896-898.

29. Qu, D. and D. Grischkowsky, *Observation of a New Type of THz Resonance of Surface Plasmons Propagating on Metal-Film Hole Arrays.* Physical Review Letters, 2004. **93**(19): p. 196804-4.

30. Nazarov, M., et al., *Surface plasmon THz waves on gratings.* Comptes Rendus Physique, 2008. **9**(2): p. 232-247.

31. Williams, C.R., et al., *Highly confined guiding of terahertz surface plasmon polaritons on structured metal surfaces.* Nature Photonics, 2008. **2**(3): p. 175-179.

32. Nazarov, M., et al., *THz surface plasmon jump between two metal edges.* Optics Communications, 2007. **277**(1): p. 33-39.

33. Mukina, L.S., M.M. Nazarov, and A.P. Shkurinov, *Propagation of THz plasmon pulse on corrugated and flat metal surface.* Surface Science, 2006. **600**(20): p. 4771-4776.

34. Zhizhin, G.N., et al., *Absorption of surface plasmons in "metal-cladding layer-air" structure at terahertz frequencies.* Infrared Physics & Technology, 2006. **49**(1-2): p. 108-112.

35. Zhang, J. and D. Grischkowsky, *Adiabatic compression of parallel-plate metal waveguides for sensitivity enhancement of waveguide THz time-domain spectroscopy.* Applied Physics Letters, 2005. **86**(6): p. 061109-3.

36. Reiten, M.T., *Spatially Resolved THz Propagation*, in *Electrical Engineering*. 2006, Oklahoma State University: Stillwater. p. 227.

37. Begley, D.L., et al., *Propagation distances of surface electromagnetic waves in the far infrared.* Surface Science, 1979. **81**(1): p. 245-251.

38. Koteles, E.S. and W.H. McNeill, *Far infrared surface plasmon propagation.* International Journal of Infrared and Millimeter Waves, 1981. **2**(2): p. 361-371.

39. Steijn, K.W., R.J. Seymour, and G.I. Stegeman, *Attenuation of far-infrared surface plasmons on overcoated metal.* Applied Physics Letters, 1986. **49**(18): p. 1151-1153.

40. Saxler, J., et al., *Time-domain measurements of surface plasmon polaritons in the terahertz frequency range.* Physical Review B, 2004. **69**(15): p. 155427.

41. Raether, H., *Surface Plasmons on Smooth and Rough Surfaces and on Gratings* 1988, Berlin Heidelberg New York London Paris Tokyo: Springer-Verlag. 136.

42. Zhao, Y. and D. Grischkowsky, *Terahertz demonstrations of effectively two-dimensional photonic bandgap structures.* Opt. Lett., 2006. **31**(10): p. 1534-1536.

43. Mendis, R., *First Broadband Experimental study of planar Terahertz Waveguides* in *Electrical Engineering*. 2001, Oklahoma State University: Stillwater.

44. Gallot, G., et al., *Terahertz waveguides.* J. Opt. Soc. Am. B, 2000. **17**(5): p. 851-863.

45. Mendis, R. and D. Grischkowsky, *Plastic ribbon THz waveguides.* Journal of Applied Physics, 2000. **88**(7): p. 4449-4451.

46. Lesurf, J.C.G., *Millimetre-wave Optics, Devices and Systems*. 1990: Adam Hilger, Bristol and New York. 251.

47. Zhao, Y. and D.R. Grischkowsky, *2-D Terahertz Metallic Photonic Crystals in Parallel-Plate Waveguides.* Microwave Theory and Techniques, IEEE Transactions on, 2007. **55**(4): p. 656-663.

48. Mendis, R. and D. Grischkowsky, *THz interconnect with low-loss and low-group velocity dispersion.* Microwave and Wireless Components Letters, IEEE, 2001. **11**(11): p. 444-446.

Appendixes

Appendix I Model analysis of dielectric coated surface

In our study, the surface waveguide structure is shown in below fig. A-1(a). h = 12.5 μm, ε_d = 2.25, and the metal underneath is assumed aluminum.

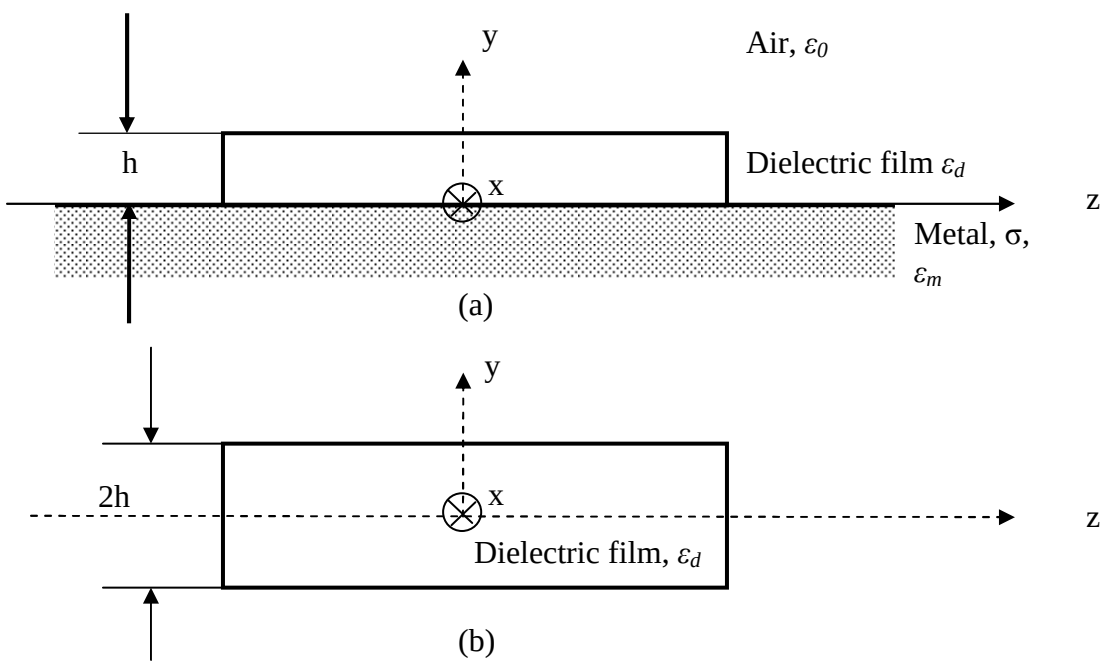

Figure A-1. Equivalent wave guiding structures

Method 1 and 2 assume in THz, aluminum is perfect electrical conductor (PEC), σ =∞.

To solve the wave equations in this structure (a), we refer to the solution in ref.[2], it is possible to first solve the wave equations in a free-standing dielectric slab waveguide of twice thickness of the same material, as shown in fig. A-1 (b), then apply the boundary condition (perfect conductor boundary at the plane of symmetry) to eliminate unsuitable modes and select the correct modes for (a)

Two methods of solving the dielectric slab waveguide are introduced here.

1. Direct wave equation method. [2]

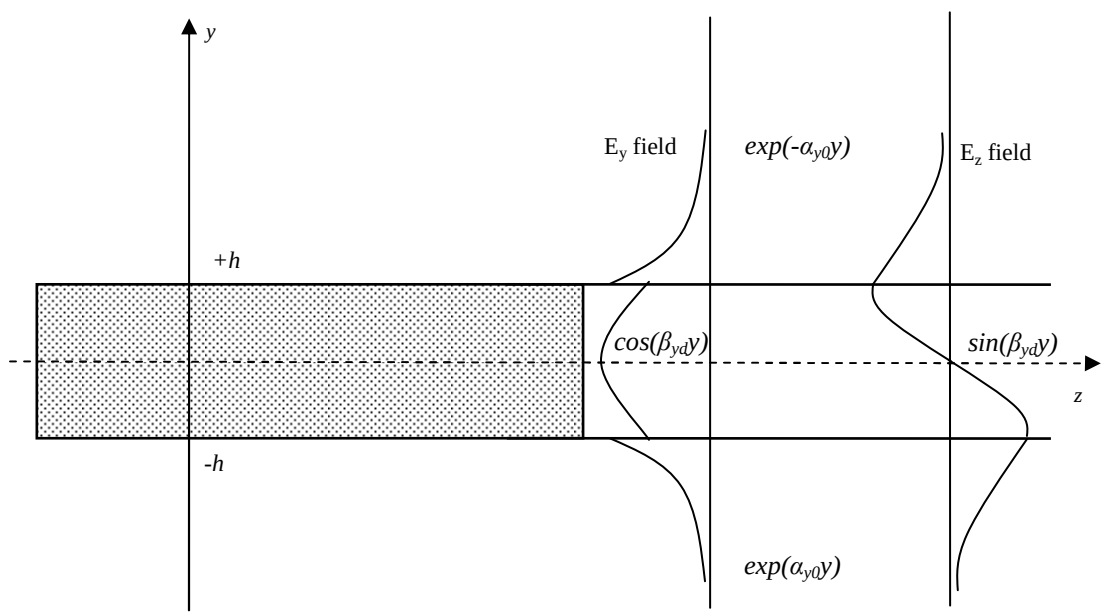

Figure A-2. Perpendicular (E_y) and tangential field (E_z) of TM_0 mode of dielectric slab waveguide[2], it should be noted that the TM_0-E_z field is much smaller ~ 0.05 than the TM_0-E_y field

The Helmholtz wave equation is used in the dielectric slab waveguide structure. The formats of the solution to the Helmholtz equation in slab structure include: TE and TM

modes. In our scope of studying, to couple free space wave into surface, it requires that the electric field vector lie within the incidence plane, therefore, only TM field need to be considered. Furthermore, because of the symmetry of the structure, the solutions have two types of symmetric modes: even and odd. As shown in fig A-2. However, with the existence of PEC plane in the center, the only allowed modes are TM even mode which satisfies the boundary condition as tangential electrical field to be zero on the PEC plane. Below figure shows the E field profile of the fundamental even mode, where the tangential field E_z is zero at the plane of symmetry. It will be discussed later that the waveguide is running under single mode (TM_0) propagation.

The field solution of TM even mode is listed below:

$$E_x^d = 0$$

$$E_y^d = -\frac{\beta_{yd}\beta_z}{\omega\mu_d\varepsilon_d} A_m^d \cos(\beta_{yd} y) e^{-j\beta_z z}$$

$$E_z^d = -j\frac{\beta_d^2 - \beta_z^2}{\omega\mu_d\varepsilon_d} A_m^d \sin(\beta_{yd} y) e^{-j\beta_z z}$$

$0 < y < h$
In the film

$$H_x^d = \frac{\beta_{yd}}{\mu_d} A_m^d \cos(\beta_{yd} y) e^{-j\beta_z z}$$

$$H_y^d = 0$$

$$H_z^d = 0$$

$$E_x^{0+} = 0$$

$$E_y^{0+} = \frac{\alpha_{yo}\beta_z}{\omega\mu_0\varepsilon_0} B_m^{0+} e^{-\alpha_{yo} y} e^{-j\beta_z z}$$

$$E_z^{0+} = -j\frac{1}{\omega\mu_0\varepsilon_0}(\beta_0^2 - \beta_z^2) B_m^{0+} e^{-\alpha_{yo} y} e^{-j\beta_z z}$$

$y > h$
In the air

$$H_x^{0+} = -\frac{\alpha_{yo}}{\mu_0} B_m^{0+} e^{-\alpha_{yo} y} e^{-j\beta_z z}$$

$$H_y^{0+} = 0$$

$$H_z^{0+} = 0$$

Where the superscript d in all field variables refer to fields inside the dielectric and 0+ is for fields in vacuum above the dielectric. A_m^d and B_m^{0+} is field amplitudes which will be evaluated at the boundary. β_z is the wave vector in propagation direction z. β_{yd} and α_{yo} are y components of wave vector inside the film and in the air, respectively. These three

parameters are unknown and have to be determined in order to have the complete wave field expression. From the above fields inside and outside the film, it can be seen that in this structure, only E_y, E_z and H_x field are not zero. In addition, inside the film the fields are trigonometric functions and outside the film they are exponential functions. By enforcing boundary conditions, the β_z, β_{yd} and α_{yo} can be determined by numerically solving the simultaneous equations below *(Eq. (8-160), (8-167) and (8-168) in ref.[2])*:

$$(\alpha_{y0}h)^2 + (\beta_{yd}h)^2 = a^2 \tag{A-1}$$

$$\frac{\varepsilon_0}{\varepsilon_d}(\beta_{yd}h)\tan(\beta_{yd}h) = \alpha_{yo}h \tag{A-2}$$

$$\alpha_{y0}^2 + \beta_{yd}^2 = \beta_d^2 - \beta_0^2 = \omega^2(\mu_d\varepsilon_d - \mu_0\varepsilon_0) \tag{A-3}$$

Where $a = \omega h\sqrt{\mu_0\varepsilon_0}\sqrt{\mu_r\varepsilon_r - 1}$

For TM even mode, the cutoff frequency is

$$(f_c)_m = \frac{m}{4h\sqrt{\mu_d\varepsilon_d - \mu_0\varepsilon_0}} \quad \text{where m = 0, 2, 4, ….} \tag{A-4}$$

Substitute $h = 25\ \mu m$, $\varepsilon_d = \varepsilon_r\varepsilon_0 = 2.25 \times 8.854 \times 10^{-12}\ F/m$, $\mu_d = \mu_0 = 4\pi\times 10^{-7}\ H/m$, we have

$$f_c = m \times 2.68\ THz$$

Therefore, for the dominant mode TM^z_0 *(m=0)*, $f_c = 0$, which means all frequency can have unattenuated propagation in this mode. For the second lowest mode *(m = 2)* is f_c = *5.36 THz*, which is higher than the highest frequency of our system. Thus TM_0 is the only mode that is allowed in our surface waveguide system.

2. Mode parameter method [1]

Another method published in Snyder and Love's book is a more general method for dielectric waveguide with symmetric structures. First it defines some dimensionless parameters base on the waveguide refractive index profile and cross-sectional geometry. Then, the quantities of interest (such as wave vectors, attenuation constants, group velocities, fraction of power in the dielectric and etc.) are worked out as expressions in Snyder and Love's notation.

Given the frequency of electromagnetic wave *f*, the half thickness of the dielectric waveguide $\boldsymbol{\rho}$ **(which equals to *h* in method 1),** the refractive index of the dielectric (core) n_{co} and the refractive index of surrounding medium (cladding) n_{cl}, we define:

1. Waveguide and fiber parameter *V (Eq. 11-47, pg.227 ref.[1])*

$$V = \frac{2\pi\rho}{\lambda}(n_{co}^2 - n_{cl}^2)^{1/2} = \sqrt{\rho^2 k^2 (n_{co}^2 - n_{cl}^2)} \qquad \text{(A-5)}$$

Where $k = \frac{2\pi}{\lambda} = \frac{2\pi f}{c}$

2. Profile height parameter *Δ (Eq. 11-48, pg.227 ref. [1])*

$$\Delta = \frac{1}{2}\{1 - \frac{n_{cl}^2}{n_{co}^2}\} \tag{A-6}$$

3. Modal parameters U_j and W_j *(Eq. 11-49, pg.227 ref. [1])*

$$\begin{aligned} U_j &= \rho(k^2 n_{co}^2 - \beta_j^2)^{1/2} \\ W_j &= \rho(\beta_j^2 - k^2 n_{cl}^2)^{1/2} \end{aligned} \tag{A-7}$$

Where β_j is the wave vector both inside and outside of the dielectric, which is the β_z in method 1, clearly we have *(Eq. 11-50, pg.228 ref. [1])*

$$U_j^2 + W_j^2 = \rho^2 k^2 (n_{co}^2 - n_{cl}^2) = V^2 \tag{A-8}$$

For TM modes, it has *(Table 12-2, pg.243 ref. [1])*

$$W_j = \frac{n_{cl}^2}{n_{co}^2} U_j \tan U_j \tag{A-9}$$

Equation (8) and (9) form up simultaneous equations and can be solved numerically.

Once U_j and W_j are solved, according to the tables on page 242 and 243 in ref. [1], the field distribution and other quantities can be calculated accordingly.

Example

Fig. A-3 is the identical result of applying the above two methods on a silicon slab waveguide. In this example, half thickness of the slab (h or ρ) is 65μm, refractive index is 3.42.

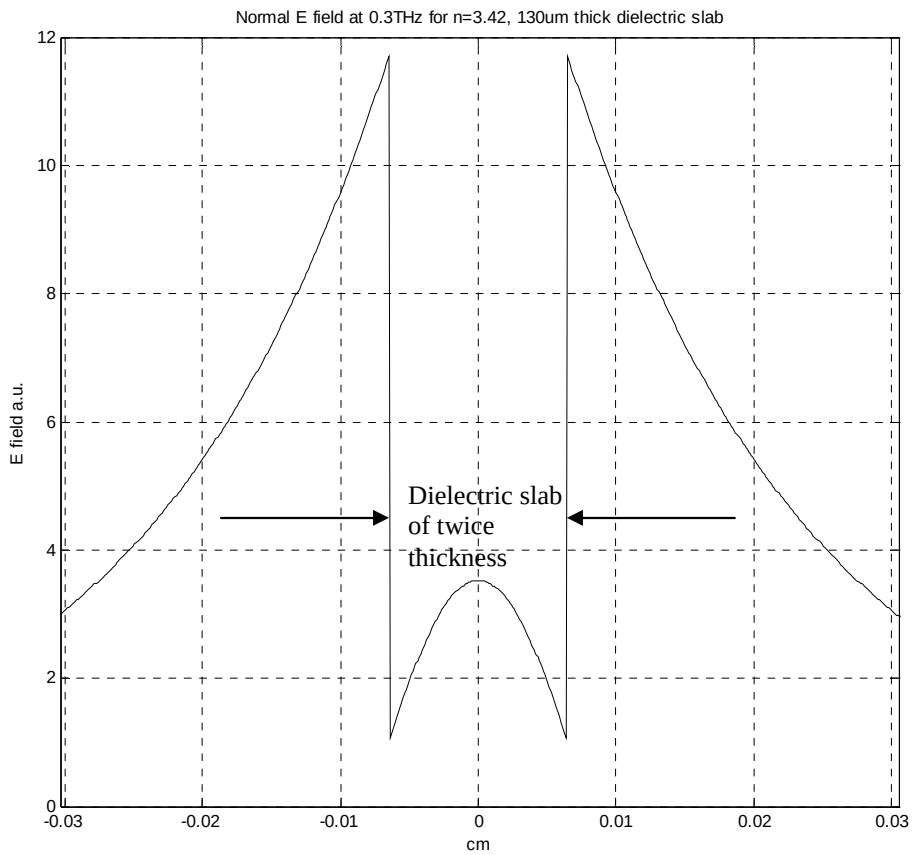

Figure A-3. Ey field distribution of TM_0^z mode in a silicon slab waveguide

From the figure, it shows the fundamental TM_0^z mode. Inside the slab waveguide, E field is a cosine function, while in the air, the field is an exponential function. Then for a 65μm silicon waveguide on PEC plane, the field distribution is just simply cut the below figure into half through the center (0 cm vertical line).

Method 3 treats aluminum as normal metal with complex dielectric constant $\hat{\varepsilon}_m$

This method was worked out by Schlesinger and Sievers [22]. In their paper, they tried to directly solve the wave equations in the surface waveguide (fig. A-1(a)) with complex

metal dielectric constant. The complex wavevector β_z is solved numerically, as given in below equation 9. Then the exponential decay constant in the perpendicular direction can also be calculated using the same relation in equation (3) in method 1.

$$\hat{\beta}_z \approx \frac{\omega}{c}\left\{1-\frac{1}{2\hat{\varepsilon}_m}+\left[\frac{(\varepsilon_d-1)}{\varepsilon_d(-\hat{\varepsilon}_m)^{-1/2}}+\frac{\varepsilon_d}{(-\hat{\varepsilon}_m)^{3/2}}\right]x+\left[\frac{1}{2}(\frac{\varepsilon_d-1}{\varepsilon_d})^2+\frac{\varepsilon_d^2}{2\hat{\varepsilon}_m^2}+\frac{2(\varepsilon_d-1)}{(-\hat{\varepsilon}_m)}\right]x^2 + \left[\frac{(\varepsilon_d-1)^2}{\varepsilon_d(-\hat{\varepsilon}_m)^{1/2}}+\frac{\varepsilon_d(\varepsilon_d-1)}{(-\hat{\varepsilon})^{3/2}}\right]x^3+\frac{(\varepsilon_d-1)^2}{2(-\hat{\varepsilon}_m)}x^4\right\} \quad \text{(A-10)}$$

Where $\hat{\beta}_z$ is the complex wave vector of surface wave, ε_d is the dielectric constant of overlayer, $\hat{\varepsilon}_m$ is the complex dielectric constant of substrate metal. At 1THz, for aluminum we have $\hat{\varepsilon}_m = -3.3\times10^4 + i6.4\times10^5$. x in the equation is $2\pi h/\lambda$. Where λ is the wavelength of surface wave, h is the thickness of overlayer and c is the speed of light. From this equation, the real part of $\hat{\beta}_z$ corresponds to the β_z calculated in method 1 and 2.

Appendix II Metal conductivity

According to simple Drude model, the frequency-dependent complex dielectric constant is given in SI units as[47].

$$\begin{aligned}\varepsilon_m &= \varepsilon_m' + i\varepsilon_m'' \\ &= \varepsilon_\infty + i\sigma_m/(\varepsilon_0\omega) \\ &= \varepsilon_\infty - \omega_p^2/\omega(\omega+i\Gamma)\end{aligned} \quad \text{(A-11)}$$

Where the corresponding Drude complex metal conductivity is given by

$$\sigma_m = \sigma_{dc} i\Gamma/(\omega + i\Gamma) = i\varepsilon_0 \omega_p^2/(\omega + i\Gamma) \tag{A-12}$$

In above equations, ε_0 is the vacuum permittivity, ε_∞ is the contribution of the bound electrons, ω_p is the plasma angular frequency and Γ is the damping rate, which is defined as $\Gamma = 1/\tau$ where τ is the average collision time.

In the optical and near infrared range, metal conductivity has small real part and big imaginary part which makes the metal lossy medium.

On the other hand, in the microwave and THz range, $\omega/\Gamma \ll 1$, as a result, the Drude complex conductivity and dielectric constant of metal can be expressed to an excellent approximation as

$$\begin{aligned} \sigma_m &\approx \sigma_{dc} \\ \varepsilon_m &= \varepsilon_m' + i\varepsilon_m'' \approx -\frac{\sigma_{dc}}{\varepsilon_0 \Gamma} + i\frac{\sigma_{dc}}{\varepsilon_0 \omega} \end{aligned} \tag{A-13}$$

Within this accurate approximation, in the THz range, the metal conductivity is equal to its handbook dc value which is very high and can be considered as ideal conductor. The real part of metal dielectric constant is a negative constant, while the much larger imaginary part is proportional to the wavelength. Therefore in the THz range, metals have high conductivity and behave like ideal lossless conductor.

Appendix III Metal absorption

1) Analytical method

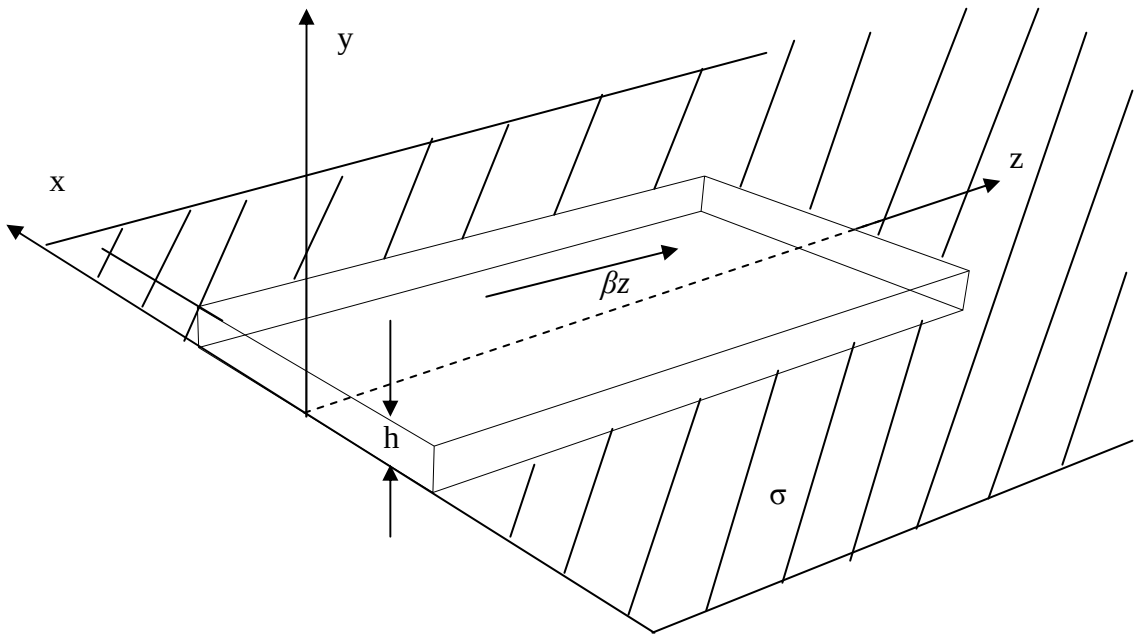

Figure A-4 Surface waveguide structures

Due to the uniformity along the x axis as shown in the above structure in fig. A-4, there are only 3 field components need to be solved in the Maxwell's equations: E_y, H_x and E_z. According to the (8-62) on ref [2], page 377, the power absorbed and dissipated as heat by the metal surface, denoted as P_c is

$$P_c = \frac{dP}{dz} = \frac{1}{2}\frac{1}{\sigma\delta} H_x^2 \Big|_{y=0} \qquad \text{(A-14)}$$

Where σ is the conductivity of the metal and $\delta \approx \sqrt{\frac{2}{\omega\mu\sigma}}$ is the skin depth of good conductor.

The power flow inside the dielectric layer P_{z1} is

$$P_{z1} = \frac{1}{2}\hat{a}_z \int_0^h \mathrm{Re}[E_y \times H_x]dy \qquad \text{(A-15)}$$

Similarly, the power flow outside the dielectric layer (in the air) P_{z2} is

$$P_{z2} = \frac{1}{2}\hat{a}_z \int_h^\infty \mathrm{Re}[E_y \times H_x]dy \qquad \text{(A-16)}$$

Therefore we have the total power flow P:

$$P = P_{z1} + P_{z2} \qquad \text{(A-17)}$$

The metal power absorption α_m is defined similar to equation 4- 9,

$$P(z) = P_0 e^{-\alpha_m z}$$

$$\alpha_m = \frac{\frac{dP}{dz}}{P(z)} \qquad \text{(A-18)}$$

Where v_l is the group velocity of bulk material and v_g is the mode group velocity within the waveguide layer. As the expression of H_x and E_y, are all known, after substituting into the above equations,

$$\alpha_m = \frac{\sqrt{\frac{\omega\mu_d}{2\sigma}}\frac{\omega\varepsilon_d}{\beta_z}}{\frac{\sin 2\beta_{yd}h}{2\beta_{yd}} + h} \cdot \eta \tag{A-19}$$

Where η is the fraction of power within the dielectric layer, $\mu_d = \mu_r\mu_0 = 4\pi\times10^{-7}$ H/m (μ_r = 1 for non-ferrites), $\varepsilon_d = n^2\varepsilon_0 = 1.5^2 \times 8.854 \times10^{-12}$ F/m, for aluminum $\sigma = 4\times10^7$ S/m β_{yd} is the wave vector in the y direction inside the film and it has:

$$\beta_z^2 + \beta_{yd}^2 = \omega^2\mu_d\varepsilon_d \tag{A-20}$$

Equation A-19 can be simplified by making some approximations. For h in μm, we have:

$$\begin{gathered} \sin 2\beta_{yd}h \approx 2\beta_{yd}h \\ \beta_z \approx \beta_0 = \omega\sqrt{\mu_0\varepsilon_0} \end{gathered} \tag{A-21}$$

Substitute the above into 20, the simplified expression of amplitude absorption $\alpha_m/2$ is:

$$\alpha_m/2 = \sqrt{\frac{\omega\mu_0}{2\sigma}}\frac{\omega n^2\varepsilon_0}{4h\omega\sqrt{\mu_0\varepsilon_0}}\eta = \sqrt{\frac{\pi c}{\lambda\sigma}}\frac{n^2\sqrt{\varepsilon_0}}{4h}\eta \approx n\eta\alpha_m^{PPWG}/4 \tag{A-22}$$

2) Approximation method

In a dielectric filled parallel plate waveguide (PPWG), as shown in below fig. A-5(a), when studying the metal loss due to the finite conductivity, our surface wave case can be

approximated that one of the metal plates has been removed (fig. A-5(b)). Under this approximation, the loss due to the finite metal conductivity can be acquired in 3 steps: First the loss is reduced to half of the loss of PPWG because there is only one metal plate. Second it needs to be multiplied by the fraction of total power within the film because the power is flowing both inside and outside the film. Third, the power is no longer propagating with the bulk dielectric group velocity (c/n) but approximately with c because the majority energy is hanging outside the film. Therefore, the velocity ratio is also needed as a correction factor [44]. From fig. 4-2 it shows that although the E field inside the film is a cosine function, for such a small thickness h compared to the wavelength, the field variation is almost flat. This can be approximated to be uniform, which is just the same as the TEM mode in PPWG.

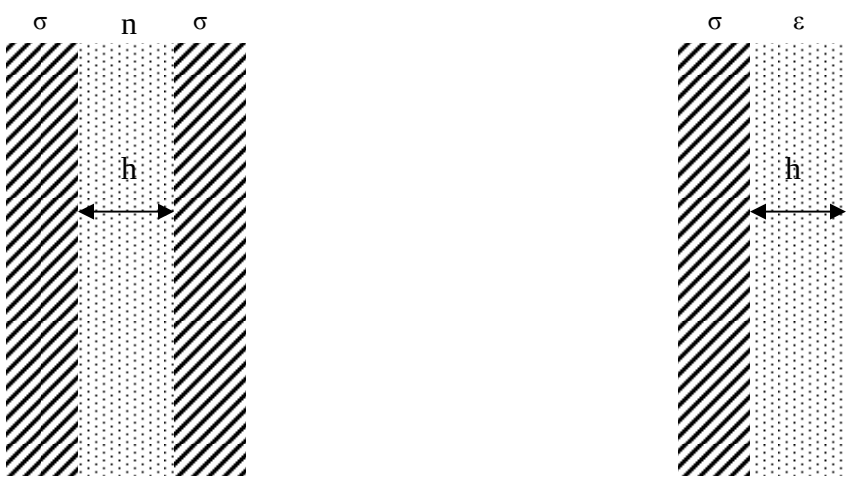

(a) (b)

Figure A-5. Using parallel plate waveguide to approximate surface waveguide

For fig. A-5(a), the metal plate amplitude loss α_m for TEM mode propagation can be written as [48], attenuation coefficient:

$$\alpha_m^{PPWG} = nR / \eta_0 h \qquad \text{(amplitude loss)} \qquad \text{(A-23)}$$

And the corresponding power attenuation coefficient is twice α_m^{PPWG}. Where n = 1.5 is the index of refraction of the dielectric, R = 10.88 $\times 10^{-3}[10^7/(\sigma\lambda_0)]^{1/2}$ for TEM mode. h = 12.5 μm is the thickness of the dielectric, σ = 4×10^7 S/m for aluminum and $\eta_0 = \sqrt{\mu_0 / \varepsilon_0} \approx 377\Omega$ is the impedance of free space.

For the surface waveguide, the amplitude loss is ½ that of the PPWG multiplied by the fraction of power η (equation (4 - 8)) within the dielectric layer of thickness h and the velocity ratio. The approximated metal amplitude attenuation coefficient in surface waveguide is:

$$\alpha_m^{SW} = 0.5\eta\alpha_m^{PPWG}\frac{v_l}{v_g} \approx 0.5\eta\alpha_m^{PPWG} / n \qquad \text{(A-24)}$$

This result gives the amplitude attenuation constant (due to the metal) of the surface wave as fig. 4-8 shows the curve of α_m^{SW} versus frequency which agrees well with the result of the original analytical method:

$$\alpha_m^{SW} = 0.5\eta\alpha_m^{PPWG} / n = 1.44\times 10^{-5}\times\sqrt{\frac{10^7}{\sigma\lambda}}\times\frac{\eta}{h} \approx 0.9(\alpha_m / 2) \qquad \text{(A-25)}$$

VITA

Gong, Mufei

Candidate for the Degree of

Doctor of Philosophy

Dissertation: STUDY OF THZ SURFACE WAVES (TSW) ON BARE AND COATED METAL SURFACE

Major Field: Electrical Engineering

Biographical:

Born in Mudanjiang, P. R. China, son of Gong, Chuan and Guan, Chun'ai.

Education:
B.S. Optoelectronics, 1998, Tianjin University, China.
M. Eng., 2001, Nanyang Technological University, Singapore.
Completed the requirements for the Doctor of Philosophy in Electrical Engineering at Oklahoma State University, Stillwater, Oklahoma in July, 2009.

Experience:
Worked as electronic designer in *3rd Research Institute of China Aerospace Science & Industry Corp. (CASIC), Tianjin, China – Aug 1998 to May 1999*

Professional Memberships:
Student Member of Optical Society of America (OSA)

Name: Gong, Mufei Date of Degree: July, 2009

Institution: Oklahoma State University Location: Stillwater, Oklahoma

Title of Study: STUDY OF THZ SURFACE WAVES (TSW) ON BARE AND COATED METAL SURFACE

Pages in Study: 84 Candidate for the Degree of Doctor of Philosophy

Major Field: Electrical Engineering

Scope and Method of Study: The focus of the research was to investigate the propagation characteristics (such as field distribution, attenuation and group velocity) of terahertz surface waves on bare and dielectric coated metal surface. The experiment was carried out on a modified standard terahertz time-domain spectroscopy system. Surface waves were coupled into the metal surface using the parallel plate waveguide coupling mechanism. The picosecond terahertz pulses were generated and detected using the Grischkowsky photo-conductive transmitter and antenna driven by a femtosecond laser.

Findings and Conclusions: Surface waves at microwave and terahertz frequencies are weakly guided on bare metal surface due to the high metal conductivity. Detailed wave coupling analysis and experiment has shown that on a bare metal surface, the majority of energy remains to be uncoupled freely propagating waves. The spatial extent of the terahertz surface wave collapses two orders of magnitude upon the addition of the sub-wavelength dielectric layer on the metal surface. Simple theory in terahertz range gives an accurate explanation to this effect. Direct experimental measurements of the terahertz surface wave on an aluminum surface covered with a 12.5 μm thick dielectric layer have completely characterized the wave. The measurements of the frequency-dependent exponential fall-off of the evanescent wave from the surface agree well with theory.

ADVISER'S APPROVAL: Dr. Daniel Grischkowsky